

Research paper

# Implosion of the Argentinian submarine ARA San Juan S-42 undersea: Modeling and simulation<sup>☆</sup>



Chunqiu Wei<sup>a</sup>, Goong Chen<sup>b,c,\*</sup>, Alexey Sergeev<sup>b</sup>, Jean Yeh<sup>d</sup>, Jianhua Chen<sup>e</sup>, Junmin Wang<sup>a</sup>, Shaochun Ji<sup>f</sup>, Jiao Wang<sup>a</sup>, Donghui Yang<sup>g</sup>, Shuhuang Xiang<sup>h</sup>, Xiaomin Cao<sup>i</sup>, Wenyng Lu<sup>e</sup>, Marlan O. Scully<sup>c,j</sup>

<sup>a</sup> School of Mathematics and Statistics, Beijing Institute of Technology, Beijing 102488, China

<sup>b</sup> Department of Mathematics, Texas A&M University, College Station, TX 77843, USA

<sup>c</sup> Institute for Quantum Science and Engineering, Texas A&M University, College Station, TX 77843, USA

<sup>d</sup> Department of Mathematics, National Kaohsiung Normal University, Kaohsiung 80201, Taiwan, Rep. of China

<sup>e</sup> School of Mathematical and Computational Science, Hunan University of Science and Technology, Xiangtan, Hunan 411201, China

<sup>f</sup> Faculty of Mathematics and Physics, Huaiyin Institute of Technology, Huai'an, Jiangsu 223003, China

<sup>g</sup> School of Mathematical and Statistics, and School of Automation, Central South University, Changsha, Hunan 410075, China

<sup>h</sup> School of Mathematics and Statistics, Central South University, Changsha, Hunan 410083, China

<sup>i</sup> School of mathematical Sciences, Shanxi University, Taiyuan, Shanxi 030006, China

<sup>j</sup> Baylor Research and Innovation Collaborative, Waco, TX 76708, USA

## ARTICLE INFO

### Article history:

Received 13 April 2020

Revised 1 June 2020

Accepted 4 June 2020

Available online 4 July 2020

## ABSTRACT

This paper studies a contemporary event of the sunken Argentinian submarine ARA San Juan S-42 in November 2017. The submarine's wreckage was found one year later on the seabed off the southern Atlantic coast of Argentina, with its imploded debris scattered on the seabed at the depth of about 900 meters under sea level. We develop computational mechanics modeling and conduct supercomputer simulations for this study, using the versatile software LS-DYNA as the platform. We first revisit underwater implosion phenomena by the test of pressurizing a plugged aluminum cylinder in a water tank and match the patterns of structural deformations as the important way to validate our computational methodology and model selections. Furthermore, the radiations of the implosion shocks are computed and compared with those in the literature. Using a base model for the submarine, we are able to perform event reconstruction for the underwater implosion of ARA San Juan S-42. Our work can encompass the features of structural fracture and break-up, which were not included in the earlier studies. Furthermore, we show that by adding ring stiffeners ("buckle arrestors"), we can delay the onset of underwater implosion by increasing the tolerance of more water depth for the submarine. All the dynamic nonlinear implosion phenomena can be visualized by video animations obtained from our supercomputer simulations, which are also compared with an artistically rendered video animation.

© 2020 Elsevier B.V. All rights reserved.

## 1. Introduction

This paper studies a contemporary event by computational modeling and simulation.

<sup>☆</sup> Dedicated to Professor Wei-Ming Ni (1950–) on the Occasion of His 70th Birthday.

\* Corresponding author at: Department of Mathematics, Texas A&M University, College Station, TX 77843, USA.

E-mail address: [gchen@math.tamu.edu](mailto:gchen@math.tamu.edu) (G. Chen).



**Fig. 1.** A photograph of the Argentinean Submarine ARA San Juan S-42 [1].

The submarine ARA San Juan S-42 of the Argentinean Navy, see Fig. 1, was on patrol off Argentina's South Atlantic coast on November 15, 2017, when it was reported missing. A search and rescue mission was launched almost immediately with the help of the International Submarine Escape and Rescue Liaison Office. On November 23, 2017, it was also reported that a signal consistent with an underwater implosion was detected by the Preparatory Commission for the Comprehensive Nuclear-Test-Ban Treaty Organization at its listening posts on Ascension Island and Crozet Islands on November 15, 2017. This is one ominous sign that the fate of the submarine may have met with its demise. On November 30, 2017, the Argentinean Navy announced that the search and rescue operation came to an end. Forty four of the submarine crew have perished.

Nevertheless, the search of the submarine wreckage on seabed had continued. On November 16, 2018, 366 days after the loss of ARA San Juan, a remote submersible operated by the Norwegian ship *Seabed Constructor* owned by the Houston, USA, company *Ocean Infinity* had found the wreckage of ARA San Juan at the depth of 907 m under water. The submarine's debris was found to have scattered over an area of about 8000 m<sup>2</sup>.

How does a submarine or a deep-dive submersible implode underwater? This question being studied here could unavoidably involve the gruesome deaths of the crew or the operators. In the preparation of this academic study, the authors trust that due attention has been paid by us to possible issues of sensitivity so that there is no show of disrespect to the victims. The motivation of this study is totally *curiosity-driven*. All the referenced materials here are available in the open literature and are unclassified. Our work is based on the computational mathematical and mechanical modeling and simulation. The work began since Summer 2018 with many participants who were visitors with the team of Dr. Goong Chen (the second and corresponding author of this paper) at the Mathematics Department of Texas A&M University. Primary supercomputer work and theoretical investigation were done by Chunqiu Wei (the lead author) as part of her PhD co-training under the supervision of Goong Chen at Texas A&M University, where her study is sponsored by the Chinese Scholarship Council.

The processes of implosion offer many interesting physical and mechanical phenomena. They manifest a *highly nonlinear* behavior where *condensation* happens in the system. Such a condensation process for a *star* can lead to a total structural collapse in astrophysics, for example, where a dying star under the gravitational pull can form a *black hole*. During the structural collapse, if the outer shell or surface of the star cannot withstand the outward counteracting force, then (implosion-induced) *explosion* can happen such as that of a *supernova*. Elsewhere, implosion has been used as a leading technology for the ignition of the first atom bomb in the Manhattan Project [2]. The concept of implosion has also been applied to the demolition of old buildings or skyscrapers by making such civil structures collapse inward into itself without affecting any neighboring building structures [3].

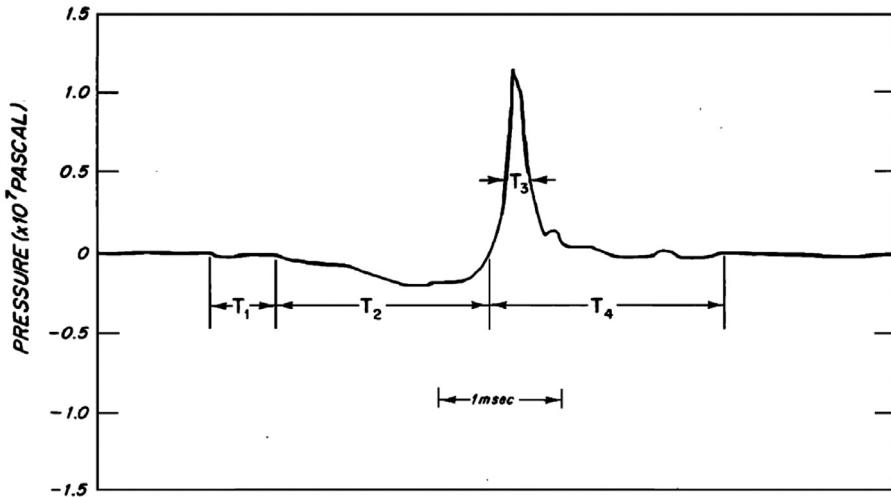


**Fig. 2.** Acoustic signature of an underwater implosion, where four time-components have been labelled as in Orr and Schoenberg [4, Fig. 4]. Initially ( $T_1$ ), the pressure is undisturbed. A drop in pressure happens in  $T_2$  during the initial collapse of structure. Then during  $T_3$ , there is a positive pressure spike. Finally, during  $T_4$ , there is a decay of pressure fluctuations as the structure collapses upon itself and the water motion is arrested. The lengths of the time durations  $T_2$ ,  $T_3$  and  $T_4$  are distinctive features of this type of underwater implosion. The pattern of a single spike and the time duration  $T_2$  are the most characteristic of this acoustic signature.

As the implosion of a submarine happens in deep, dark water, virtually nobody has ever seen its occurrence *in situ*. But such an event, in principle, is no different from the examples of implosions mentioned in the preceding paragraph. The only extra ingredient is *water* as the medium. When a submarine malfunctions and sinks to ever larger depths, the increasing water pressure as a function of water depth exerts correspondingly higher hydrostatic pressure on the outer shell of the submarine. As soon as the buckling or safety structural thresholds have been crossed, implosion happens abruptly, within the order of several milliseconds (*ms*) in time, and the outer shell is severely deformed or crushed. This is a totally nonlinear dynamic process. This implosion also triggers the radiation of pulses, releasing energy in the form of an acoustic shock. Such a shock, or a series of such shocks, can do serious damage to nearby underwater structures; see the accident at the Super-Kamiokande facility in Japan in November 2001 [5].

For the study of underwater implosion, some of the early work can be traced back to 1858 [6]. Much of the earlier work emphasized the applicational aspect regarding the determination of external pressure that could cause the collapse of thin-walled structures such as boilers, penstocks, vacuum tanks and other similar structures. Analytically, such problems were treated as classical nonlinear (linearized) stability problems in elasticity and plasticity.

But after the work of Issacs and Maxwell [7] in 1952, the acoustic signatures of underwater implosion have caught the attention of researchers [4,8]. It was first pointed out by Orr and Schoenberg [8] that underwater implosion's acoustic signatures have the four time-components as shown in Fig. 2.

The work in [4] signified that the fluid dynamic aspects were also important and, methodologically, underwater implosion must be studied as a *fluid-structure interaction (FSI)* problem. From the physics point of view, it was also found that the *implosion event is similar to the collapse of cavitation and underwater explosion bubbles* [9–16].

Computational fluid dynamics (CFD)-based models for FSI have been developed in Kamran [17], Farhat et al. [18], for example; see also the references therein, together with finite element method (FEM) based schemes or others and numerical examples showing agreements with experiments. Such work has provided a solid foundation for our work here. Nevertheless, *fracturing and breakup* were not covered in their models and computations. For the topic of submarine implosion, we note that there have not been many scholarly research articles in the open literature. This topic, we believe, carries some sensitivity involving national defense or military armament issues, which may have lead to certain classified status for many of such studies. Our publication here, thus, could very well *claim priority* on submarine undersea implosion in the open literature, *by default*. However, it is a pleasant surprise that a 4-minute movie/video has been made by Kostack Studio [19] to animate the implosion of ARA San Juan S-42 by using the advanced visualization software *Blender* [20]. The visual effects in [19] are indeed lively and vivid, garnering more than two million viewers in YouTube. This is really commendable. Nevertheless, a word of caution must be given is that the mathematical procedures and methods for Hollywood-style artistic rendering are *not based on the first principles of mechanics*. Therefore, as such, even though the visualization in movies looks real, the phenomena therein are different, sometimes to a large extent, from reality. This has already been pointed out in an earlier paper [21]. In this paper, we will dedicate a subsection expressly for the purpose of making comparisons of manifested phenomena between computer-modeling and movie-making.

The coupling between the 3D fluids (seawater + air) and solids (submarine), due to the complex shape of the submarine, cannot be decoupled. Therefore, the governing equations, the equations of state, the boundary/interface conditions, and other

physical constraints altogether form a large system of coupled PDEs, whose mathematical analysis is, theoretically, mostly intractable. Hence, here in this paper, our main work is focused *mainly on modeling and computation*. Our methodology is *software based, on LS-DYNA*, which is, to our knowledge, the most advanced in treating macroscopic damage and fracture problems. LS-DYNA is a commercial software whose codes are inaccessible to the users. This is a major restriction for many large scale computational projects. There are a number of novel aspects of the present work, as follows:

- (1) Our approach is computational modeling, which is comprehensive and can help theory-building;
- (2) We are able to visualize the nonlinear dynamics of the implosion process by video animations, using the state-of-the-art software;
- (3) Our models and simulations naturally include the fracture mechanical features, which were mostly absent in previous work;
- (4) We are able to provide an extensive set of graphical comparisons between computational mechanics and artistically rendered movies, which might eventually help movie-making look even more realistic;
- (5) Our work can facilitate future underwater vehicle designs to better withstand implosions in deep water.

The rest of this paper is organized as follows.

In [Section 2](#), we present the fundamentals of computational modeling for underwater implosion;

In [Section 3](#), we revisit important phenomena of pattern-formation for the implosion of underwater cylindrical shells and use them to validate our work of modeling and supercomputer simulation;

In [Section 4](#), we first make a base model of the submarine ARA San Juan S-42 and demonstrate the dynamic effects of how it could have imploded undersea. Then, as an application we show that ring-stiffeners can help a submarine withstand implosion in increased depth, and show some details of the implosion process;

In [Section 5](#), we make comparisons between our visualization effects and those based on movie-style artistic rendering;

The final [Section 6](#) offers concluding remarks for this study. Technical details of computational modeling and computer codes are given in the Appendices.

Modern nuclear submarines (for example, U.S. Los Angeles-Class, Russian Typhoon-Class, etc.) are known to have double hulls, inner and outer, which can enhance deterrence against underwater implosion. Therefore, for our work to be generalized to such modern classes of submarines, this must be taken into account. But, San Juan S-42 had only a single hull [\[1\]](#). Overall, the authors have tried to build the submarine model for San Juan S-42 with their best efforts. Nevertheless, there remains too much information whether regarding the mechanical designs or material properties that is unavailable to us in the open literature either due to classification of military secrecy, or others. Therefore, our study here should be viewed, to a good extent, as *exploratory*, rather than a definitive, investigative account and a final say on this submarine tragedy. This type of work is highly interdisciplinary and can obviously benefit from cross examinations by experts in related professions such as material science, damage mechanics and marine/naval architecture, and by continued work in the sequels. We really hope to motivate further interests on the topic and to promote better safety designs for future deep-dive underwater vehicles.

## 2. Mathematical modeling of underwater implosion

In this section, we first revisit some earlier models for underwater implosion. Then we describe our own computational model.

Much of the theoretical modeling work is clear for this study as an FSI problem: There is a body of fluid, i.e., water. Suspended inside the water is a (usually thin-walled) solid with cavity, filled with air within the cavity. The fluids and solids motions are coupled by the usual kind of *interface conditions*. We are investigating, under what conditions when the water pressure acting on the solid increases, how the solid will undergo structural collapse and/or disintegration. Thus, mathematically, we can describe the model given in the next subsections.

### 2.1. Review of a prior model

Historically, the study of underwater implosion began as an extension of the physics of the collapse of cavitation and underwater explosion bubbles due to their mutual similarities. For the modeling of cavitation, air and water as the two involved fluids, are both often modeled as *compressible*. (At least, the air must be modeled as compressible.) Thus, in preceding studies [\[17,22,23\]](#), for example, a compressible, inviscid system of Euler equations is proposed. Specifically, let  $\Omega_F(t) \subset \mathbb{R}^3$  denote the fluid domain of interest, that is, the union of the domains  $\Omega_w(t)$  and  $\Omega_a(t)$  of water and air, respectively. The governing Euler equations can be written in conservation form as

$$\frac{\partial \mathbf{W}}{\partial t} + \nabla \cdot \mathbf{F}(\mathbf{W}) = 0 \quad \text{in } \Omega_F, \quad (\Omega_F(t) = \Omega_w(t) \cup \Omega_a(t)),$$

where  $t$  denotes time;  $\Omega_w(t)$ ,  $\Omega_a(t)$  and  $\Omega_F(t)$  are time-varying domains, and

$$\mathbf{W} = (\rho, \rho v_x, \rho v_y, \rho v_z, E)^T, \quad \nabla = \left( \frac{\partial}{\partial x}, \frac{\partial}{\partial y}, \frac{\partial}{\partial z} \right)^T,$$

$$\mathbf{F}(\mathbf{W}) = (F_x(\mathbf{W}), F_y(\mathbf{W}), F_z(\mathbf{W}))^T,$$

$$F_x = \begin{Bmatrix} \rho v_x \\ P + \rho v_x^2 \\ \rho v_x v_y \\ \rho v_x v_z \\ v_x(E + P) \end{Bmatrix}, \quad F_y = \begin{Bmatrix} \rho v_y \\ \rho v_x v_y \\ P + \rho v_y^2 \\ \rho v_y v_z \\ v_y(E + P) \end{Bmatrix}, \quad F_z = \begin{Bmatrix} \rho v_z \\ \rho v_x v_y \\ \rho v_y v_z \\ P + \rho v_z^2 \\ v_z(E + P) \end{Bmatrix}, \quad (2.1)$$

$\rho$  denotes the fluid density, and  $E$  is its total energy per unit volume,  $P$  denotes the fluid pressure, and  $v = (v_x, v_y, v_z)^T$  is its velocity vector.

Complementing the above conservation law, one also needs the empirical laws of equations of state (EOS) for air and water:

(air)

$$P = (\gamma_a - 1)\rho e_a, \quad ([18, p.2951]) \quad (2.2)$$

(water)

$$P = (\gamma_s - 1)\rho e_w - \gamma_s P_s, \quad ([18, p.2951]) \quad (2.3)$$

where  $e_a$  and  $e_w$  denote, respectively, the internal energy per unit mass for air and water,  $\gamma_a$  is the ratio of specific heats for air,  $\gamma_s$  is an empirical constant experimentally determined to be 4.4, and  $P_s$  is a constant depending on molecular attraction, with  $P_s = 87,000 \text{ psi}$  (600 MPa) ([18, p. 2951]).

The equations of motion for the nonlinear elastoplastic structure  $\Omega_s(t)$  (that lies as the division between water and air, and is time-varying) are

$$\rho_s \frac{\partial^2 \mathbf{u}}{\partial t^2} = \nabla \cdot (\boldsymbol{\sigma} + \boldsymbol{\sigma} \nabla \mathbf{u}) + \mathbf{b}, \quad \text{on } \Omega_s(t), \quad (2.4)$$

where  $\mathbf{u}$  denotes the displacement vector,  $\boldsymbol{\sigma}$  is the second Piola-Kirchhoff stress tensor,  $\mathbf{b}$  is the body force acting on  $\Omega_s(t)$ , and  $\Omega_s(t)$  denotes the spatial domain occupied by the flexible structure at time  $t$ .

In the case of no fracture, there are no penetrations between surfaces so the interaction between the fluid subsystem (2.1) and the structure subsystem (2.4) are driven by two transmission conditions:

$$(\mathbf{v} - \frac{\partial \mathbf{u}}{\partial t}) \cdot \mathbf{n}_w = 0, \quad \text{on } \partial \Omega_w(t), \quad ([18, p.2951]) \quad (2.5)$$

where  $\partial \Omega_w(t)$  is the water and structure interface, depending on  $t$ ,  $\mathbf{n}_w$  is the unit outward normal to  $\partial \Omega_w(t)$ , and

$$(\boldsymbol{\sigma} + \boldsymbol{\sigma} \cdot \nabla \mathbf{u} + \mathbf{PI}) \cdot \mathbf{T} = 0 \quad \text{on } \partial \Omega_w(t), \quad ([18, p.2951]) \quad (2.6)$$

where  $\mathbf{I} = (\delta_{ij})$  with  $\delta_{ij}$  being the Kronecker delta, and  $\mathbf{T}$  is the traction tensor due to the extenal forces whose origin is not due to the flow.

## 2.2. Computational modeling based on LS-DYNA

The model in Section 2.1 posed in earlier references [17,18,22,23] has helped the present authors understand key issues raised about underwater implosion. As valuable and helpful as [17,18,22,23] are, however, our model and modeling work are different from these references in the following key aspects:

- (i) The *pressurization process* in [18] is achieved in a pressure water tank by forcing compressed air/gas into the tank. The local fluid pressure is, thus, equal to the sum of the water pressure and that of the air/gas.

In order to model such an effect, the water as a fluid should be assumed to be compressible. Thus, the compressible Euler equation in [17,18,22,23] looks to be self-consistent.

- (ii) Our approaches to pressurization are based on the *prescription of pressure in initial and boundary conditions* of the water (Appendix A.2.2). It is known that water compresses about a few percent at 50 bar (500m in depth), so it is essentially *incompressible* within the range of either submarine's operation or experimental pressurizer tests. However, in an underwater implosion event, water should be assumed to be *compressible*.

### 2.2.1. Equations of motion

Recognizing the essence of water's compressibility as above, we thus now adopt the standard compressible Navier-Stokes second order PDE system as our model for water:

$$\frac{\partial \mathbf{v}}{\partial t} + \mathbf{v} \cdot \nabla \mathbf{v} = -\nabla p + \frac{1}{Re} \Delta^2 \mathbf{v} + \frac{1}{3} \tilde{\mu} \nabla (\nabla \cdot \mathbf{v}) + \mathbf{f}, \text{ on } \Omega_w(t), \quad (2.7)$$

where  $\mathbf{v} = \mathbf{v}(\mathbf{x}, t)$  is the Eulerian velocity vector of water at point  $\mathbf{x}$  at time  $t$  within the water-occupied domain  $\Omega_w(t)$ , which depends on time  $t$ ,  $Re$  is the Reynolds number,  $\tilde{\mu}$  is the dynamic viscosity, and  $\mathbf{f}$  is the body force per unit mass. Note that the *equation of state* (to be given in the next subsection) now supersedes the incompressibility condition  $\nabla \cdot \mathbf{v} = 0$ . For the air contained within the flexible structure  $\Omega_s(t)$ , it satisfies the standard conservation laws of mass, momentum and energy, within the domain  $\Omega_a(t)$  (which denotes the domain occupied by air). Thus, air is treated as a compressible fluid. The structure occupies the domain  $\Omega_s(t)$ . Its equation of motion is essentially (2.4) as  $\Omega_s(t)$  is a viscoplastic solid. Nevertheless, in our modeling based on LS-DYNA, Eq. (2.4) is mathematically replaced by some shell models, to be specified later.

### 2.2.2. Empirical relations: equations of state

For air pressure, with air as a perfect gas, we have

$$p = (\gamma - 1) \frac{\rho}{\rho_0} E, \quad (\text{here, } E = \text{internal energy}) \quad (2.8)$$

where

$$\gamma = \frac{c_p}{c_v} \quad (\text{ratio of specific heats}). \quad (2.9)$$

Eq. (2.8) is the same as (2.2).

For water, we use following simple equation of state

$$P = C_0 + \left( \frac{\rho}{\rho_0} + 1 \right) C_1, \quad (2.10)$$

where  $C_1$  is volume modulus for water which was set to 2.25 GPa (between 2.15 to 2.25 by different sources) and  $C_0$  is a reference pressure (it could be set arbitrary because in our case the hydrostatic pressure is initialized using other LS-DYNA keywords). This linear dependence is justified as long as the compressed level of water is much less than a few percent.

### 2.2.3. ALE: Arbitrary Lagrangian-Eulerian solver [24,25]

The Navier-Stokes fluid (2.7) is assumed to behave as a *laminar* flow. (There will certainly be some *locally weak turbulent flow* near the fluid-structure interface during the short periods of implosion tests. Thus, such an assumption will lead to computational errors. Nevertheless, our numerical results in Section 3.2 supports that such errors seem to be tolerable.) For a laminar flow, LS-DYNA [24] handles the convection term in (2.7) by *local advection* and generates new mesh for the deformed material. Such a local advection follows the trajectory of motion of particles and is of the Lagrangian character. It can avoid the problem of dealing with the distortions of mesh that is completely fixed in space, i.e., the Eulerian character of the computation. Thus, the ALE solver makes the Lagrangian and Eulerian methods *coupled*. However, in LS-DYNA, no turbulence modeling is used, and its ALE cannot model boundary layer effects.

### 2.2.4. Interface/transmission conditions

According to Lysmer and Kuhlemeyer [26], Cohen and Jennings [27] and [28, p. 619], for the stress tensor  $\sigma$ , we have

$$\sigma_{normal} = -\rho c_d \mathbf{V}_{normal}, \quad (2.11)$$

$$\sigma_{shear} = -\rho c_s \mathbf{V}_{tan'}, \quad (2.12)$$

where  $\rho$ ,  $c_d$  and  $c_s$  are the material density, dilatational wave speed, and the shear wave speed of the transmitting media respectively. The magnitudes of these stresses are proportional to the particle velocities in the normal,  $\mathbf{V}_{normal}$  and tangential,  $\mathbf{V}_{tan'}$  directions. The material associated with each transmitting segment is identified during initialization so that unique values of the constants  $\rho$ ,  $c_d$  and  $c_s$  can be defined automatically.

We note that (2.5) and (2.6) are specific cases of (2.11) and (2.12), respectively, as they mean to denote the normal and shear components of the stress tensor  $\sigma$  under the governing Eq. (2.2).

### 2.2.5. Contact conditions ([26,27])

Contact conditions are set by \*CONTACT\_AUTOMATIC\_SINGLE\_SURFACE, which is the most common contact option for crash analysis. Please see the instructions in [29, p. 11-22].

### 2.2.6. Fracture criteria ([29, Manual Vol.I, p. 11–58])

- $p \geq p_{\min}$  where  $p$  is the pressure (positive in compression), and  $p_{\min}$  is the pressure at failure.
- $\sigma_1 \geq \sigma'_{\max}$ , where  $\sigma_1$  is the principal stress, and  $\sigma'_{\max}$  is the principal stress at failure.
- $\sqrt{\frac{3}{2}}\sigma'_{ij}\sigma'_{ij} \geq \bar{\sigma}_{\max}$ , where  $\sigma'_{ij}$  is the deviatoric stress component, and  $\bar{\sigma}_{\max}$  is the equivalent stress at failure.
- $\epsilon_1 \geq \epsilon_{\max}$ , where  $\epsilon_1$  is the principal strain, and  $\epsilon_{\max}$  is the principal strain at failure.
- $\gamma_1 \geq \gamma_{\max}$  where  $\gamma_1$  is the shear strain, and  $\gamma_{\max}$  is the shear strain at failure.
- The Tuler-Butcher criterion,

$$\int_0^t [\max(0, \sigma_1 - \sigma_0)]^2 dt \geq K_f.$$

The “Failure Strain” (FS) for eroding elements in the card \*MAT\_PLASTIC\_KINEMATIC is used to restrict the cracking to a specific extent.

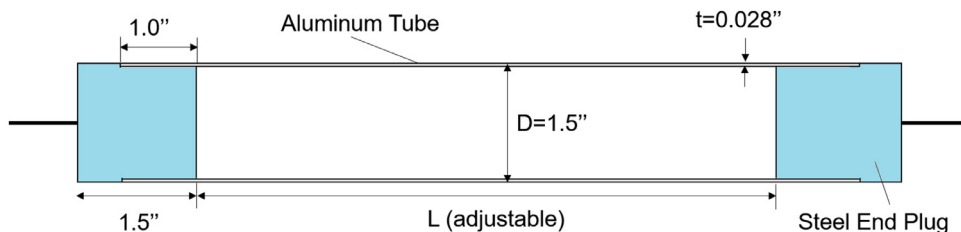
The above, Sections 2.2.1–2.2.6, constitute the mathematical model for the problem under study.

## 3. Pattern formations as bifurcations of a test aluminum cylinder in experimental underwater implosions; validation

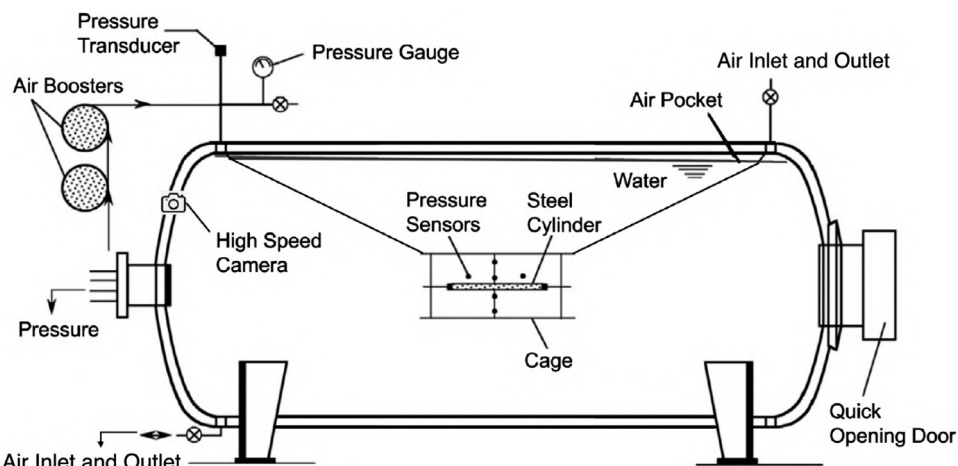
This section is intended to give a quick survey of related work so we can test our own computer modeling and simulation for the ultra important work of *validation*.

### 3.1. A quick survey with some commentaries

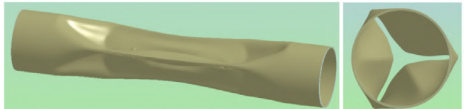
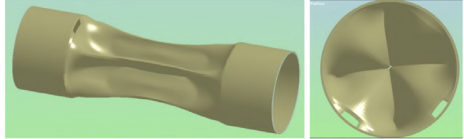
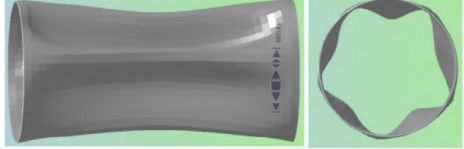
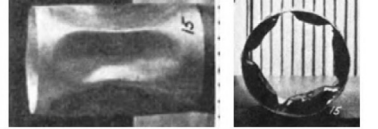
Aluminum-made cylinders plugged at both ends by steel spigots were tested in pressurized water tanks for underwater implosion by several researchers [17,18,22,23,30–36]. As the experiments done by Farhat et al. [18] are the most systematically documented, we will perform our study by following along similar lines of the approaches given in that paper. The scale, make-up and schematic of a cylinder specimen is shown in Fig. 3, while that of the pressure water tank is shown in Fig. 4. PCB piezoelectric pressure sensors are also placed around the test cylinder. As noted in the preceding section, pressurization on the cylinder inside the water tank is achieved by injecting highly pressurized air into the water. The aluminum cylinder is placed in a pressurized water tank. The set up of the apparatus and instrumentation is shown in Fig. 4. Farhat



**Fig. 3.** A plugged aluminum cylinder used by Farhat et al. [18] for the experiment of underwater implosion (adapted from [18, Fig. 3(a)]).



**Fig. 4.** Schematic of pressure water tank and instrumentation, where an aluminum cylinder is fixed and suspended in the middle, for the experimental study of underwater implosion. (Adapted from Farhat et al. [18, Fig. 1]).

Patterns	$L/D$ ratio	Our computational results	Graphical results from the literature
(a) 2-mode	8		 cf. [18, 33]
(b) 3-mode	3.5		 cf. [17]
(c) 4-mode	2		 cf. [23]
(d) 5-mode	2		 cf. [30]

**Fig. 5.** Pattern-formations of (a) 2-mode; (b) 3-mode; (c) 4-mode, and (d) 5-mode of an imploded hollow aluminum cylinder. For each pair of graphics in the above, the right one of the pair denotes a cross-sectional view from a cut at mid-length. Please note that in experimental tests as offered on the rightmost column of this table, the materials and castings may not be the same for all case (a)–(d). For example, for case (d), the specimen does not have steel plugs on both ends.

et al. [18] indicated that when the water vessel's inside pressure achieve 676 psi, for the ratio  $L/D = 2$  (where  $L$  is the length of (the cavity part of) the cylinder, while  $D$  represents the diameter of the cylinder), implosion happens on the test cylinder and its structure collapses into a 4-mode shape; see the rightmost column in Fig. 5 corresponding to the 4-mode, where a cross-sectional view of the test tube at its central-length point shows a 4-lobe pattern. Different patterns of the imploded aluminum cylinder can happen; see the mode shapes in Fig. 5. These patterns constitute the *bifurcated states* of nonlinear elastoplasticity with respect to the ratios of  $L/D$ .

### 3.1.1. Imploded test cylinder with fissures

Even though the numerical schemes in [18, 22, 23] did not include features for modeling fracture and break-up, a photo of a fractured test cylinder was displayed in [22, Fig. 19], which we reproduce here in Fig. 6. Our computation (with method-

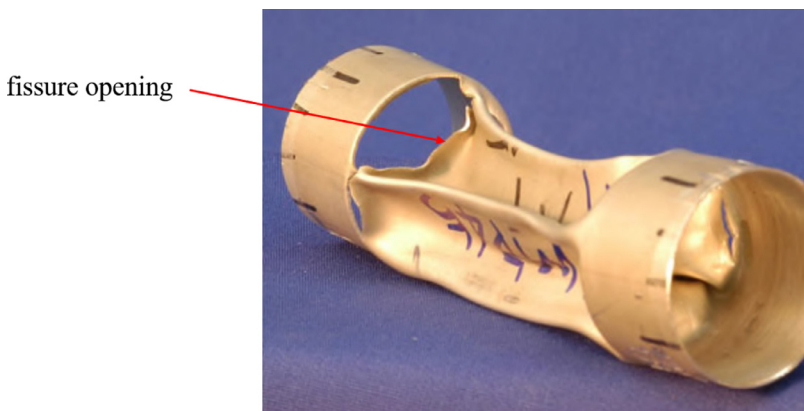


**Fig. 6.** A fractured test cylinder (adapted from [22, Fig. 19]). This appears to be a 4-mode. This deformation pattern is consistent with that given in Fig. 7, and the one in part(c) of Fig. 5. However, now there is a fissure opening.

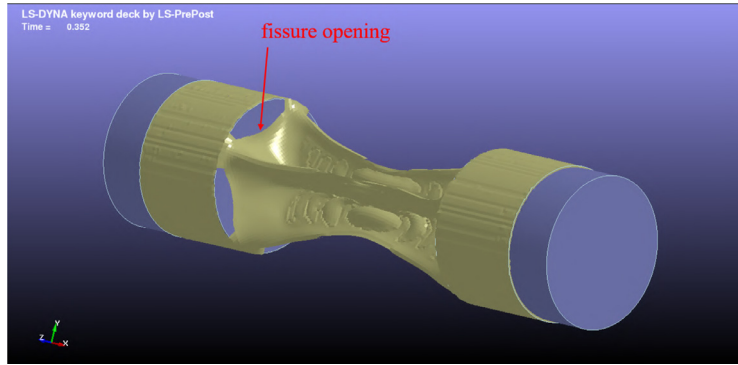


**Fig. 7.** This fractured aluminum cylinder is obtained by applying dry pressure to case (c) in Fig. 5. Note that fracture happens along the line of the aluminum cylinder-steel plug contact.

ology given in Section 3.2) is able to capture the fracture effects; see Fig. 7. The two patterns of fissures in Figs. 6 and 7, in our opinion, are rather consistent.

**Remark 1.** This two illustrations point to the assessment that in an implosion, fissure openings tend to happen along ridges and edges of a geometrical shape.

### 3.1.2. Pressure impulses

The pattern-formations so far in this section provide important benchmarks for verifying underwater implosions. Just as importantly as these distinctive patterns are the *pressure impulses* generated by the implosion. The physics of underwater implosion is known to be similar to the collapse of cavitation and underwater explosion bubbles. The pressure time series from an underwater implosion is observed to have several primary characteristics. Sequentially, an initial pressure drop in the surrounding fluid during the initial collapse, corresponding to the inward rush of the surrounding fluid. This is then followed by a subsequent positive pressure rise and fall as the body collapses upon itself and the water motion recedes. These are quite observable in Fig. 2.

In Farhat et al. [18, Fig. 6], implosion pressure signals were shown (cf. Fig. 12 in our paper), which were further compared with their numerically simulated results in [18, Fig. 17], demonstrating strong agreements.

Such pressure impulses need to be validated for our computational modeling as well. This will be carried out in Section 3.2.

### 3.1.3. Graduated implosion of a sinking long structure underwater

In the examples and graphics shown in the preceding subsections, the test specimens or structures under study were small in size and, thus, every point of the outside boundary of the structure was subject to water pressure of essentially the same magnitude. The implosion of such structures seems to happen *globally* at once on the structure. However, the implosion *does not have to happen globally at the same time* for the entire structure.

Consider a long structure of ellipsoidal shape sinking vertically in water, as shown in Fig. 8. It is known that normally for each increase of depth by 10 m in water, there is correspondingly an increase of water pressure by 1 bar. Thus, here due to the large value of length of 60 m, the bottom tip of the structure is subject to water pressure 6 bar more than that of the top tip. However, in order to make our computational work easier and the visualization effects more *dramatic*, we assume that the *body force* (acceleration) of water is 10 g rather than 1 g ( $= 9.8 \text{ m/sec}^2$ ), so that for each increase of water depth by 10 m, the corresponding increase of water pressure is 10 bar. Therefore, now the bottom tip of the structure is subject to 60 bar more than that of the top tip. Hence the leading bottom part of the structure will begin to implode first. As the full body continues its course of sinking to ever larger depths, we see graduated implosion happening from bottom to top, as shown in the panels of Fig. 8. Thus, it offers an example for the *propagation of implosion*.

## 3.2. Computational modeling by LS-DYNA and validation

### 3.2.1. Simplified computation without water: “dry” implosion

We first note that the bifurcated pattern formations as shown in the rightmost column of Fig. 5 can be computed directly as a *solid mechanics problem*, namely, by setting in (2.6) a uniform pressure force  $P$  on  $\partial\Omega_s(t)$  so that (2.6) now reads

$$(\boldsymbol{\sigma} + \boldsymbol{\sigma} \cdot \nabla \mathbf{u}) \cdot \mathbf{n} = -P \mathbf{n}; \quad (3.1)$$

where  $\mathbf{n}$  is the unit outward normal on the boundary of the shell (Fig. 9).

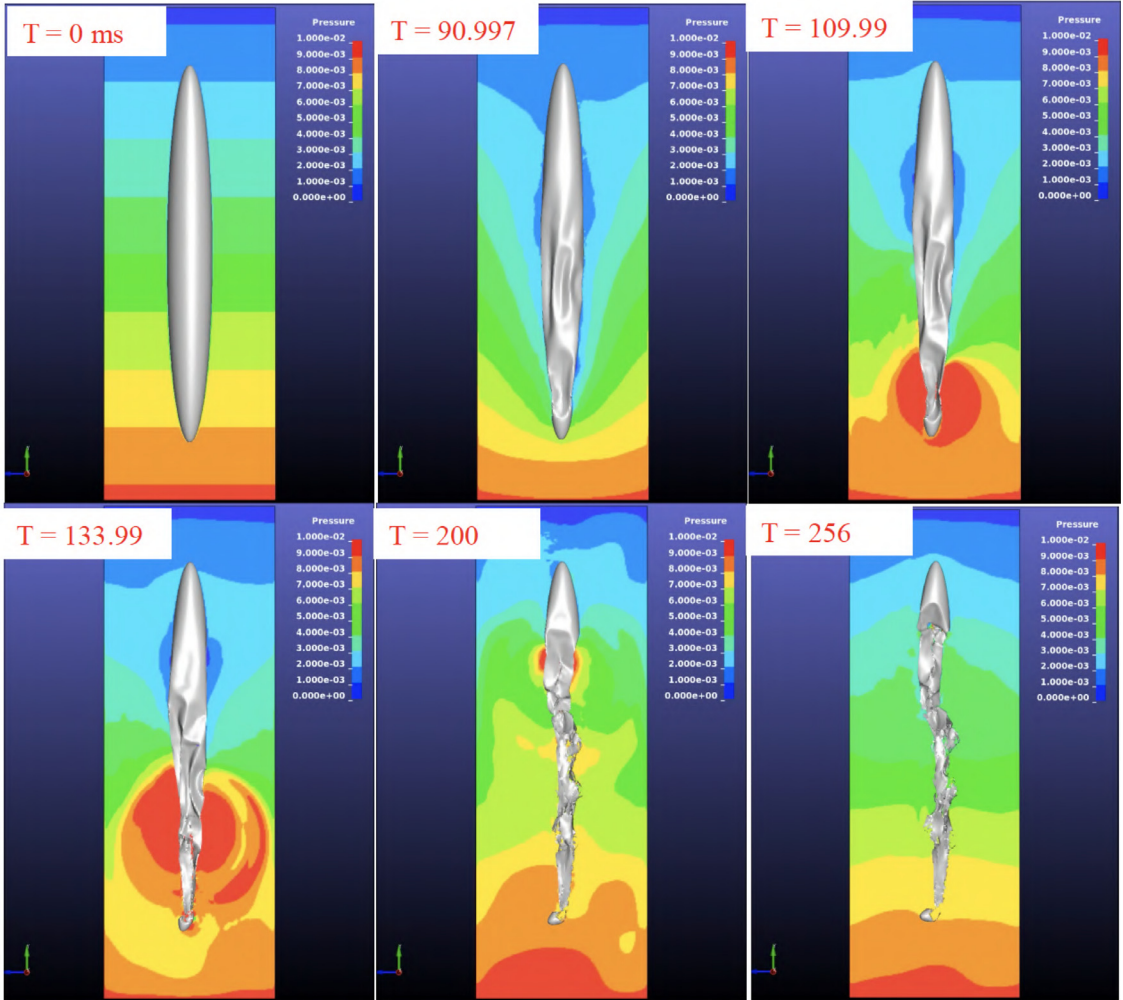


**Fig. 8.** The panels show the graduated implosion phenomenon. An ellipsoidal structure of length 60 m is sinking in water. The body force's acceleration of the fluid is assumed to be 10 g instead of the usual  $g = 9.8 \text{ m/sec}^2$ . Its bottom tip is subject to 60 bar more hydrostatic pressure than that of the top tip. One can clearly see that implosion happens first at the leading bottom part of the structure, and then moves upward, causing the eventual global implosion of the structure. Colors represent the ambient pressure. See video animation at [https://1drv.ms/v/s!Alu8\\_wrOtHEkhBKCaxalOwwFDbLX?e=SXMvXu](https://1drv.ms/v/s!Alu8_wrOtHEkhBKCaxalOwwFDbLX?e=SXMvXu).

Then for pressure  $P$  large enough, the computation will yield a buckled state, shown as one of the deformed structures on the third column of Fig. 5 according to different ratios of  $L/D$ . Such a computed state does not need to involve water as the ambient fluid. We can, thus, nickname it a *dry imploded state*.

Our formulations do not actually use (2.4) as the equations of motion, rather we have chosen a shell model. Here, we describe our model selection and computation by quoting the LS-DYNA models from [29, p. 2626]. The keyword \*SECTION\_SHELL\_TITLE is used to set the thickness and other section properties for shell elements (e.g. aluminum test cylinder or submarine). And we choose the default shell formulation “Belytschko-Tsay” [28, p. 180].

We use \*LOAD\_SHELL\_SET\_ID to apply boundary pressure with the corresponding specific keywords and choices of parameters given in Appendix A. The technical details of this LS-DYNA modeling, along with more modeling work for other relevant computations, are compiled and given in the Appendices.

By executing the computer codes on the supercomputer, we have obtained the *dry imploded states* as shown in the third column of Fig. 5.

We now have obtained a *fractured solid* (in addition to those non-fractured ones listed in column 3 of Fig. 5) resulting from applying dry pressure as in Fig. 5, case (c); see Fig. 7.

Being able to construct imploded states by using a simplified, “dry” model as above is helpful. However, this simplified way can not capture hydro-implosion impulses underwater. To do this, one must include the ambient water in order to make an FSI model, as noted in Section 3.1.2.

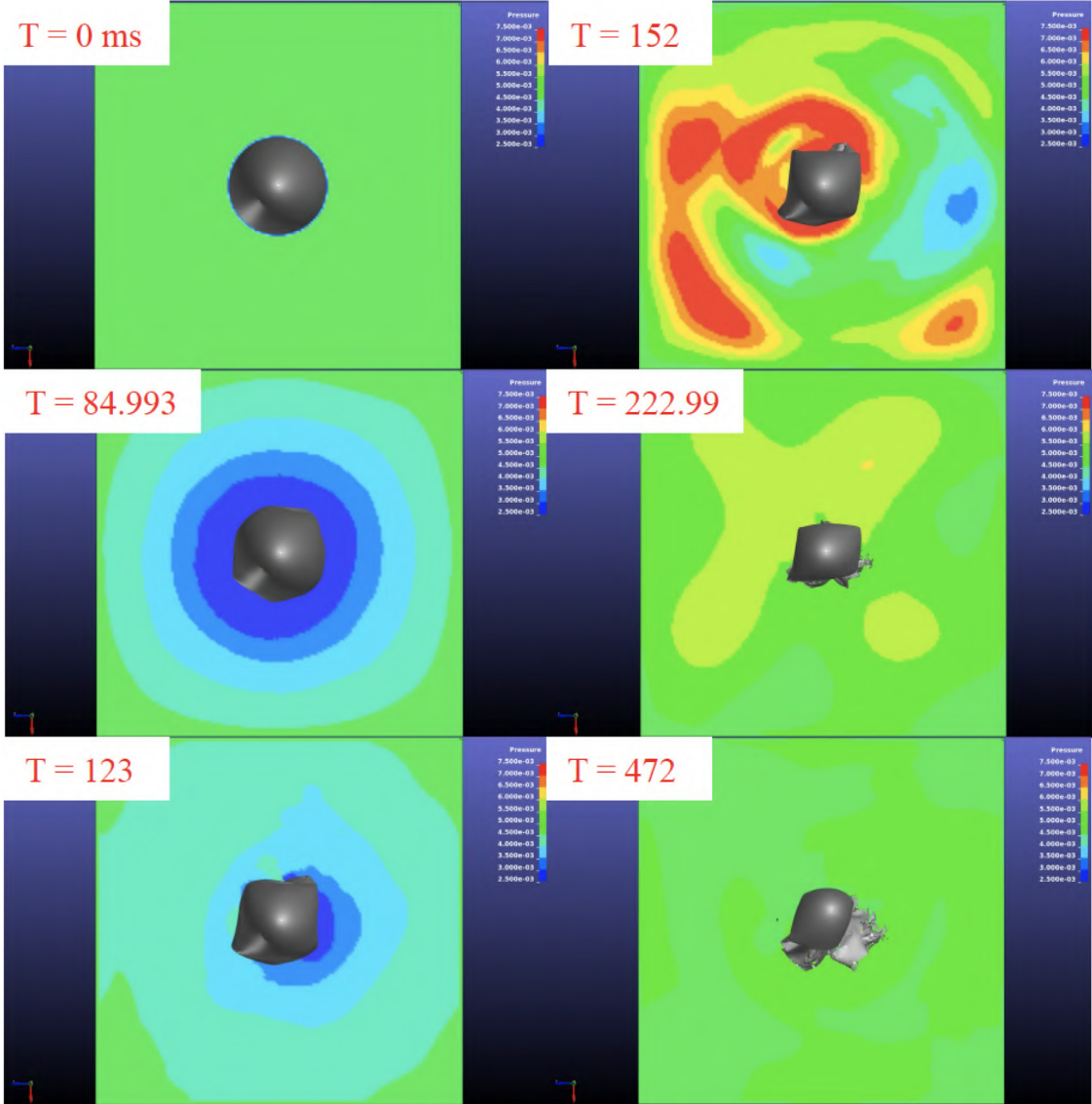


**Fig. 9.** These panels show, as a top view, the magnitude of hydrostatic pressure of the graduated implosion as described in Section 3.1.3 and Fig. 8. For video animation, see [https://1drv.ms/v/s!Alu8\\_wrOtHEkhBPyBeNy8HsGHKUD?e=cYaaZN](https://1drv.ms/v/s!Alu8_wrOtHEkhBPyBeNy8HsGHKUD?e=cYaaZN).

### 3.2.2. The geometry and meshing of the water tank

We are now ready to discuss our own FSI model. The spatial domain containing water and the immersed aluminum cylinder is chosen as in Fig. 10(a), wherein its mesh of Lagrangian finite elements is generated by using the LS-PrePost.

### 3.2.3. Pressurization of the water tank

Note that the sinking motion of a submarine or any structure engenders the increase of ambient pressure on the submarine. This is essentially a *pressurization process*. The sinking motion and the consequent increase of pressure are hard to simulate in an experimental setting or in a simulated computer modeling environment. In order to incorporate this pressurization effect in the mathematical model, an extra, somewhat artificial condition needs to be further added to represent

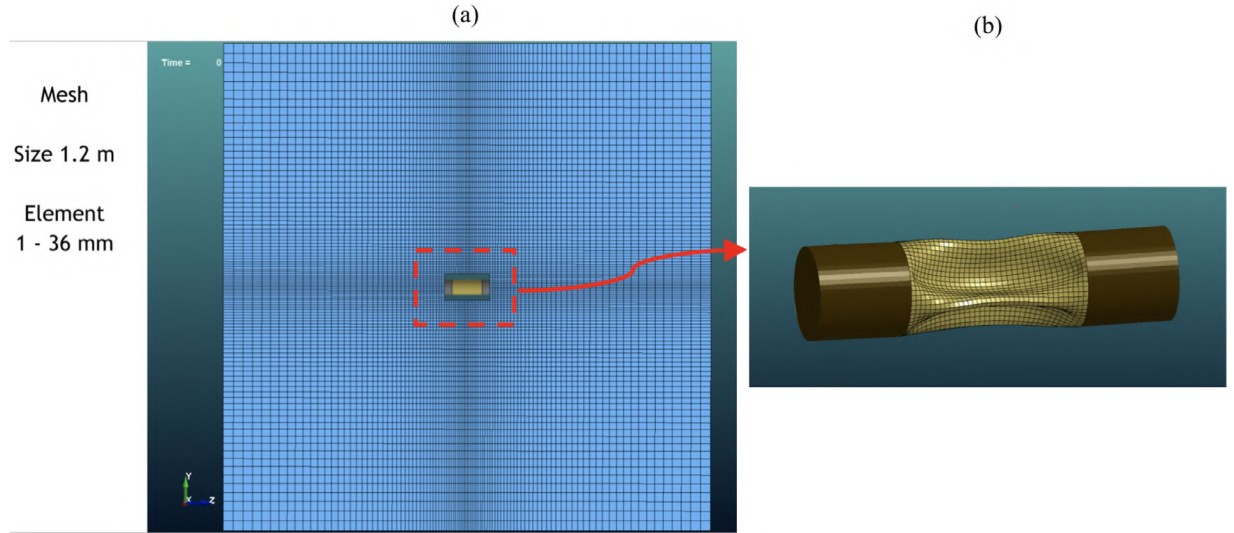


**Fig. 10.** An aluminum cylinder with air inside and steel plugs at both ends is submerged but fixed in a water tank. The water tank has dimension  $1.2 \text{ m} \times 1.2 \text{ m} \times 1.2 \text{ m}$ . It contains 1,172,872 elements as shown in part(a). Part(b) represents a locally magnified view.

the increase of pressure due to the sinking motion. In [18], this pressurization is achieved by first setting the water tank pressure to

$$P_w^0 = P_{c0} + P_a^0 - 10 \text{ psi}, \quad ([18, p.2954, leftcolumn]) \quad (3.2)$$

and then increase the pressure by injecting compressed air.

The way how (3.2) was carried out in [18] should be fine for the water tank implosion test, but may not be appropriate for the submarine implosion problem because that way of pressurization is not necessarily faithful to the physics. In our work, we achieve pressurization by assuming

(P1) initially, the pressure throughout the water tank is uniformly set to be the same, at value  $P$ ;

or

(P2) there is a top-down compressive force exerted from a “top lid of the water container”, in the form given by Fig. 11;

or

(P3) we set the pressure on the lateral boundary and bottom of the computational rectangular spatial domain as

$$P = P_0 + \rho gh, \quad (3.3)$$

where  $\rho$  is the water density,  $g = 9.8 \text{ m/sec}^2$ , and  $h$  is the water depth. For details, see Appendix C.2.

The pressurization scheme (P3) is most suitable for the computation of submarine implosion, while (P1) and (P2) are only good for the water tank implosion test problem.

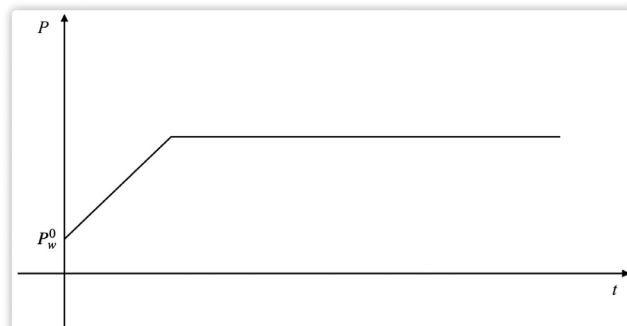


**Fig. 11.** The pressurization curve, which represents the pressure force exerted by the top lid of the water tank across all the top water surface.

### 3.3. Implementation; pressure impulses

We can now proceed to implement the computation of our model and test cylinders in, respectively, Sections 2.2 and 3.2 on the supercomputer. The basics of LS-DYNA model selections and solvers are given in the Appendices.

First, we compute the underwater implosion pattern formations (a), (b), (c) and (d) as given in Fig. 5. The computed deformed states are in strong agreement with those shown on Column 3 of Fig. 5 (obtained earlier in “dry” implosion), offering strong support to the correctness of our underwater (“wet”) implosion modeling and computation.

But the verification of the patterns of the crushed test cylinders makes up only half of the validation process. The other half, regarding underwater implosion shock impulses, is just as important (if not more so) in need of validation.

Here, we consider a 4-mode underwater implosion, case(c), in Fig. 5. We use the mesh as shown in Fig. 10(a). Pressure is recorded at 6 sensor locations as given in [18, Figs. 5(a) and (b), upper-right corner] around the mid-span of the test cylinder.

Once again, such calculations and recordings are repeated, but with the mesh halved in each dimension from that in Fig. 10(a).

The pressure impulse time series at sensor locations 1 and 3 are now overlaid on the corresponding graphics from [18], as shown in Fig. 12.

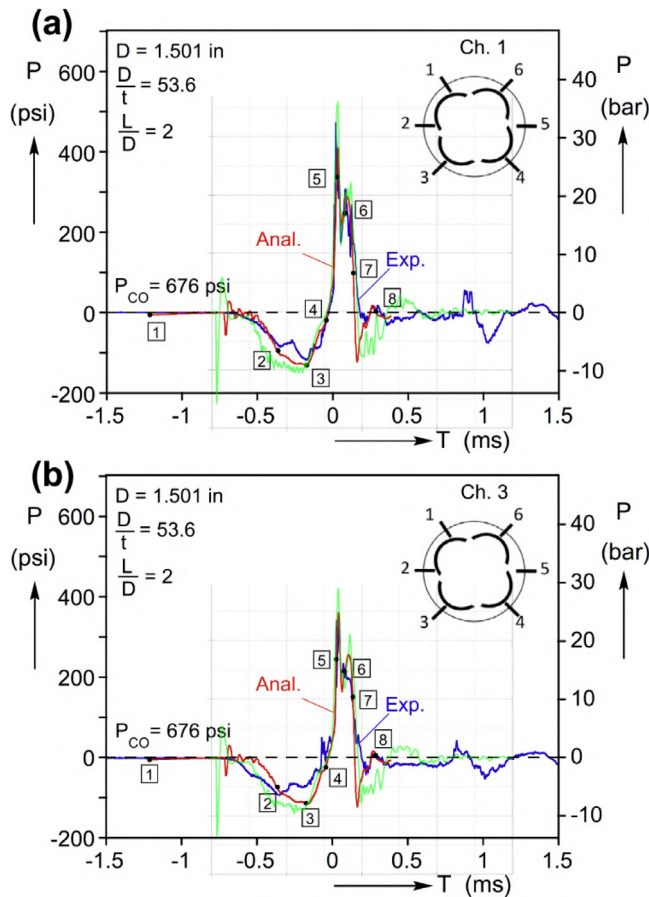


**Fig. 12.** Comparison of implosion pressure impulses between our computed ones and those of Farhat et al. [18], where there are three curves of time series:

Blue: experimental result from Farhat et al. [18], with  $T_2 = 0.797 \pm 0.01 \text{ ms}$ ,  $T_3 = 0.206 \pm 0.015 \text{ ms}$  for sensor 1;

Red: computational result from Farhat et al. [18], with  $T_2 = 0.694 \pm 0.02 \text{ ms}$ ,  $T_3 = 0.323 \pm 0.01 \text{ ms}$  for sensor 1;

Green: computational result by us, with  $T_2 = 0.76 \pm 0.015 \text{ ms}$ ,  $T_3 = 0.205 \pm 0.015 \text{ ms}$  for sensor 1.

(see definitions of  $T_2$  and  $T_3$  in Fig. 2.)

The agreements look quite consistent. For further details of our computations and comparisons, please see Appendix B. (For interpretation of the references to color in this figure legend, the reader is referred to the web version of this article.)

**Table 1**

Material properties and dimensional parameters of ARA San Juan, excerpted from [1]. For the hull and the ring-stiffeners of the submarine, the steel type HY-100 is chosen, for the reason that it is one of the most extensively used types of steel in marine structure and offshore technology. Its namesake HY-100 means it is a *high yield* steel with minimum yield strength of 100 ksi. While many steels offer high yield strength, HY-100 also offers exceptionally high impact strength as well, making it suitable for defense applications. Its carbon content is 0.1–0.2% [38].

Dimentional parameters		
Length Elastic Parameteres (HY-100)	Beam	Draught
Density 7748 kg/m <sup>3</sup>	Poisson's Ratio 0.30	Yield Stress 0.69 GPa
Young's Modulus 207 GPa	Target Modulus 67 GPa	Hardening Parameters 0.45

#### 4. The simulation of submarine implosion

A CAD model of a TR-1700-class diesel-electric submarine, to which the ARA San Juan S-42 belongs, is given by Mr. Jaramillo in [37]; see Fig. 13. Our study here is largely based on this CAD model.

##### 4.1. A base model

We first construct a FEM model of ARA San Juan based on [1,37] given in Fig. 14.

The submarine's outside metal skin is modeled as a thin steel shell with its interior filled with air. The material and structural properties can be found in Table 1. The type of steel, chosen to be HY-100, is quite commonly adopted for submarines and deep-dive vehicles, especially for submarines of the vintage of ARA San Juan. This choice of steel is natural but we have to concede that the actual steel type is unknown to us.

This base model of submarine is subject to hydrostatic pressure of 10 bar (at the depth of about 100 m underwater). It imploded after just a few milliseconds; see Fig. 15 and the video animation given in its caption.

We have tried to determine at what minimum depth, the submarine would implode. It appears that the base-model submarine would implode with pressure around 2 – 3 bar in the case of a very thin hull. This corresponds to water depth of 10 – 20 m, but implosion could thus happen only after several seconds which is a very long time for the onset of implosion. So far, this study to determine the minimal depth of implosion is inconclusive.

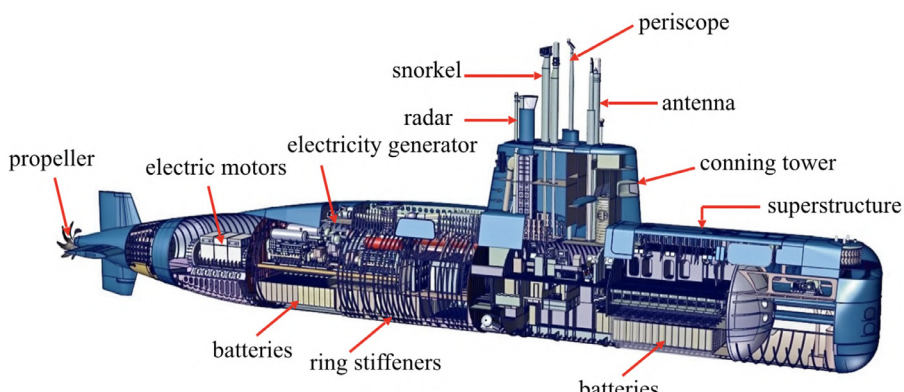


**Fig. 13.** A full geometric layout of ARA San Juan S-42 CAD modeled by Jaramillo [37], with permission.

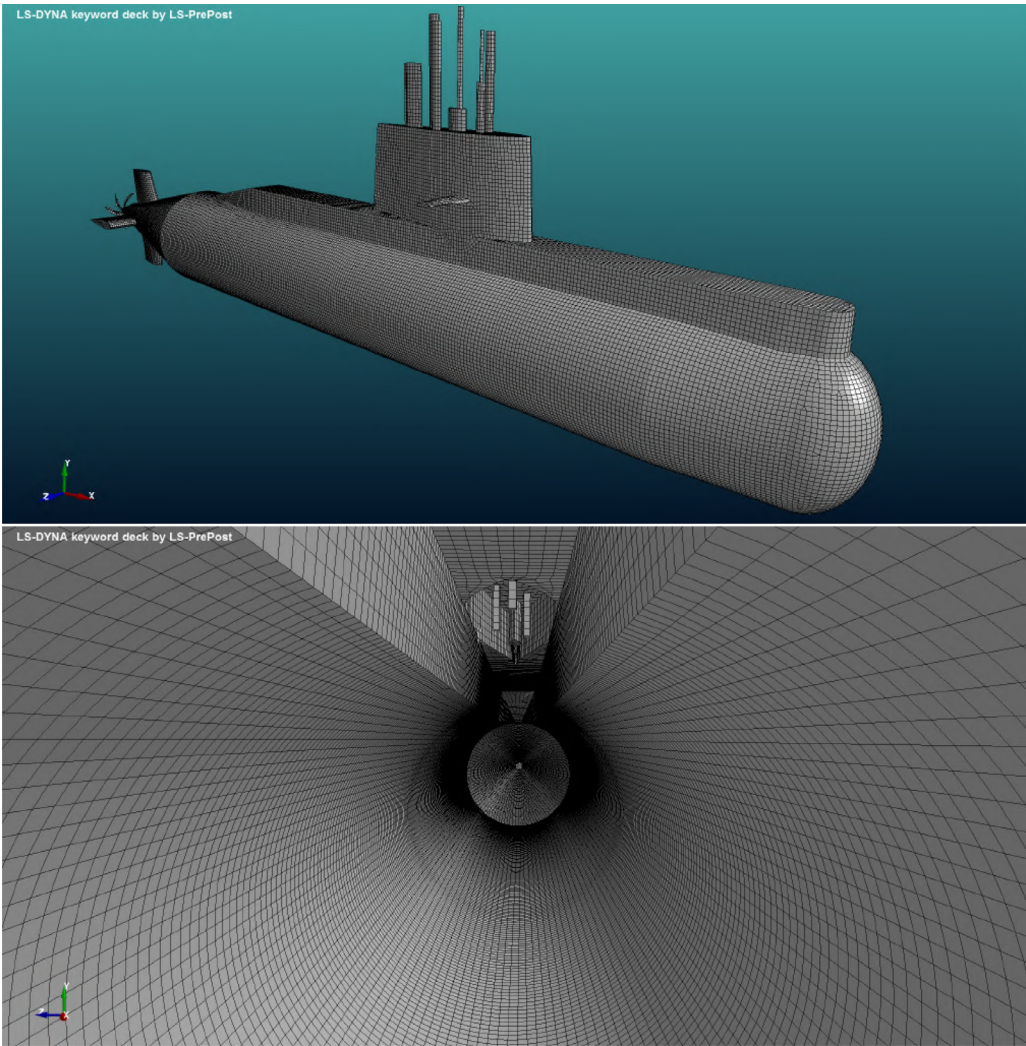


**Fig. 14.** A finite element model for the metal hull, periscope and antenna of ARA San Juan, herein a total of 88,325 Lagrangian finite elements are used, with a total of 87,881 vertices. The meshes on the outside and inside are shown, respectively, in the upper and lower panels.

#### 4.2. A submarine with ring-stiffeners: Can they delay the onset of the submarine's underwater implosion?

The base model in the preceding [Section 4.1](#) is crude; its computation is meant to serve only as “a proof of concept”. Simulation of a full-scale model of submarine *with complete interior*, see [Fig. 13](#), would require a much larger memory storage and CPU time on Texas A&M University’s campus supercomputer, which is currently beyond the scope of the paper.

However, it is well known that ring-stiffeners installed at regular intervals in an underwater long-pipe structures have an effect of arresting buckling propagation along the long pipe structure. Thus, ring stiffeners on submarines serve as “buckle arrestors” for their protective effects. In this section, we add *ring stiffeners* to the base model in [Section 4.1](#) in order to achieve more faithful modeling and also to see if they can actually delay the onset of underwater implosion. Furthermore, we add two boxes and spheres with hollow interiors ([Fig. 18](#)).

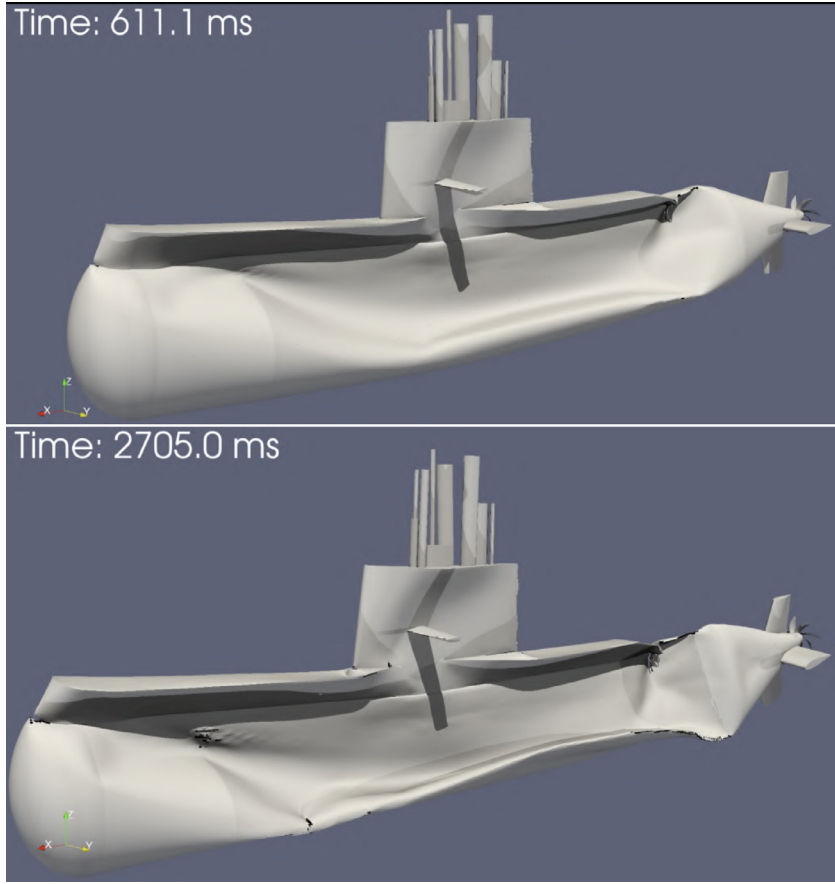


**Fig. 15.** This represents the outcome of a submarine implosion subject to 10 bar water pressure where the submarine does not have any ring stiffeners or supporting structures inside. The *port* and *starboard* sides of the submarine appear to have been squashed into contacting with each other. This damage breakup pattern should be compared against those shown in Figs. 19 and 22. For video animation, please see [https://1drv.ms/v/s!Alu8\\_wrOtHEkhEflxDpdx8AGZBdn?e=f77l8C](https://1drv.ms/v/s!Alu8_wrOtHEkhEflxDpdx8AGZBdn?e=f77l8C).

A set of ring stiffeners and stringers with spacings as given in [37] with a total number of 45 rings now have been added to the inside hull of ARA San Juan, as shown in Figs. 16 and 17. The thickness of the ring stiffeners and stringers we use is 0.2 m, and the thickness of steel is only 4 cm, i.e. the stiffeners are hollow. The material type remains to be the HY-100 steel with material parameters given in Table 1.

At the depth of 100 m (the one we computed regarding the case *without ring-stiffeners* in the preceding Section 4.1), this submarine (with ring-stiffeners) does not implode. Nor does it implode at depths of 200 m or 300 m. Here in this subsection, we use the water depth as about 500 m. So the corresponding hydrostatic pressure here is about 50 – 51 bar.

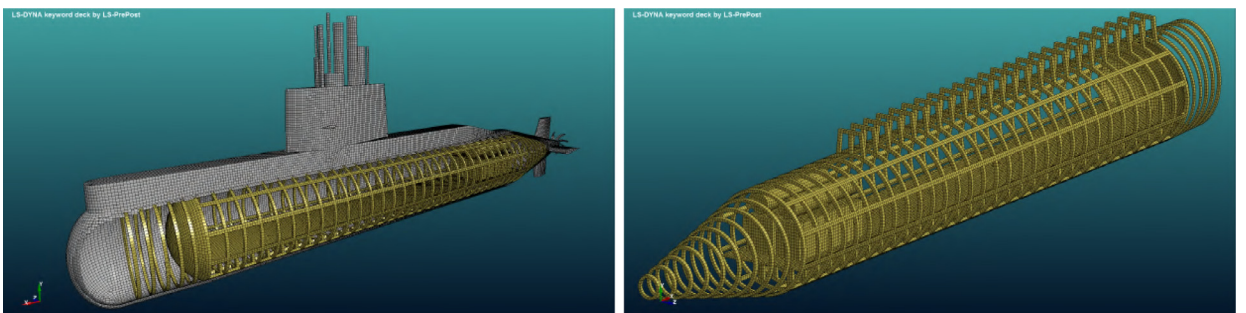


**Fig. 16.** The FEM model in Fig. 13 has now been fitted with ring stiffeners, and stringers.

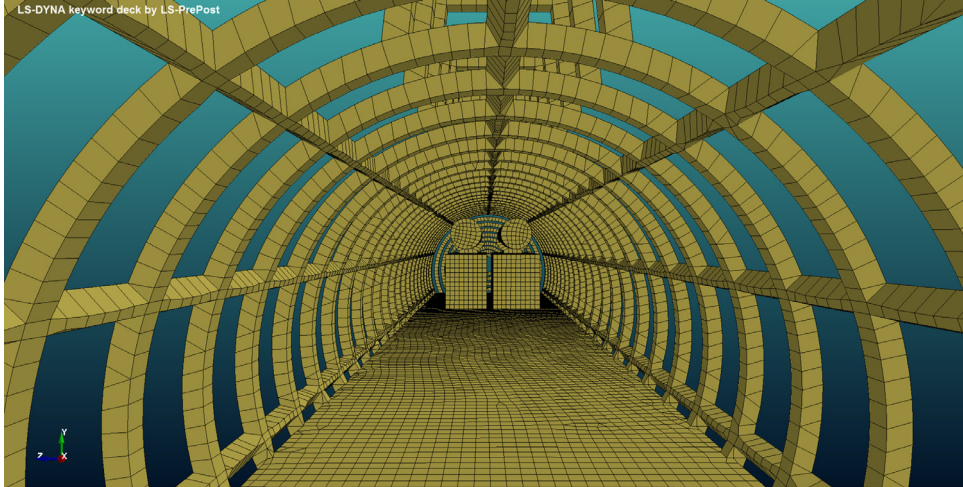


**Fig. 17.** An internal view of the shell of the submarine which is fitted with 45 ring-stiffeners, and stringers. Also, two boxes and spheres have been placed near the end of the cabin (aft section) symbolically representing some submarine inside content.

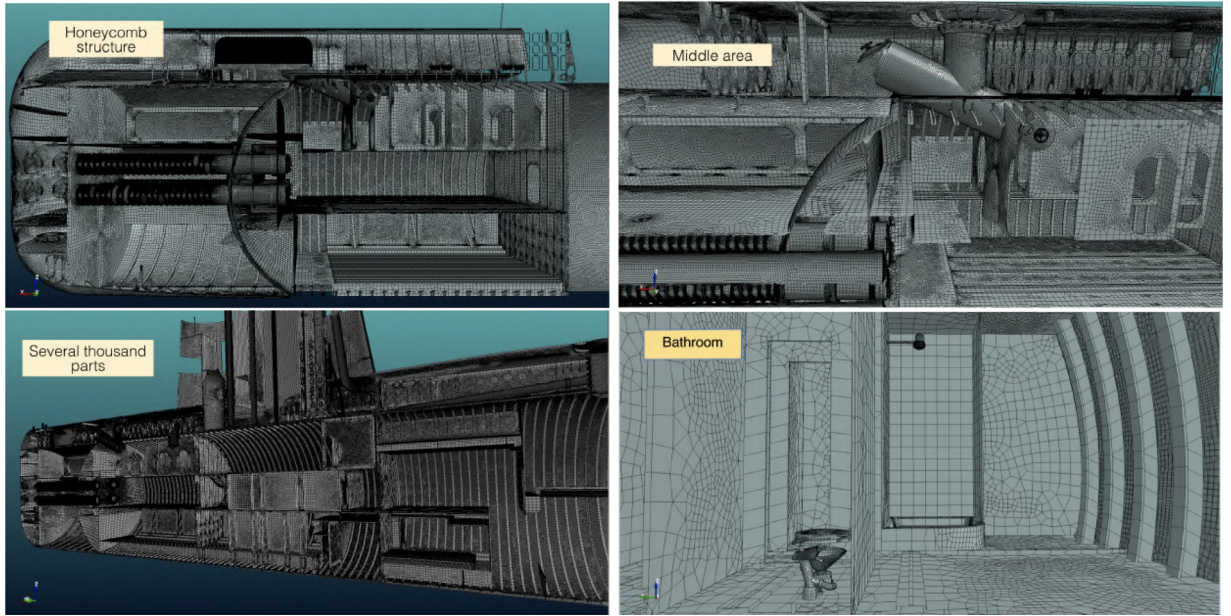


**Fig. 18.** These four panels are finite element meshings of some interior parts of ARA San Juan S-42 by LS-PrePost according to Jaramillo [37]. (Nevertheless, we are unable to use them in our supercomputer calculation due to the limitation of allocated computer memory storage on Texas A&M University's campus supercomputer.).

In Fig. 19, we show a dynamic sequence of graphics that illustrate a submarine (strengthened by ring-stiffeners) implosion in progress. Further more, in the video given in the caption of Fig. 19, we show the very same event, but with five different viewpoints:

- (i) exterior view
- (ii) stress intensity view
- (iii) transparent view
- (iv) interior view
- (v) skeletal view

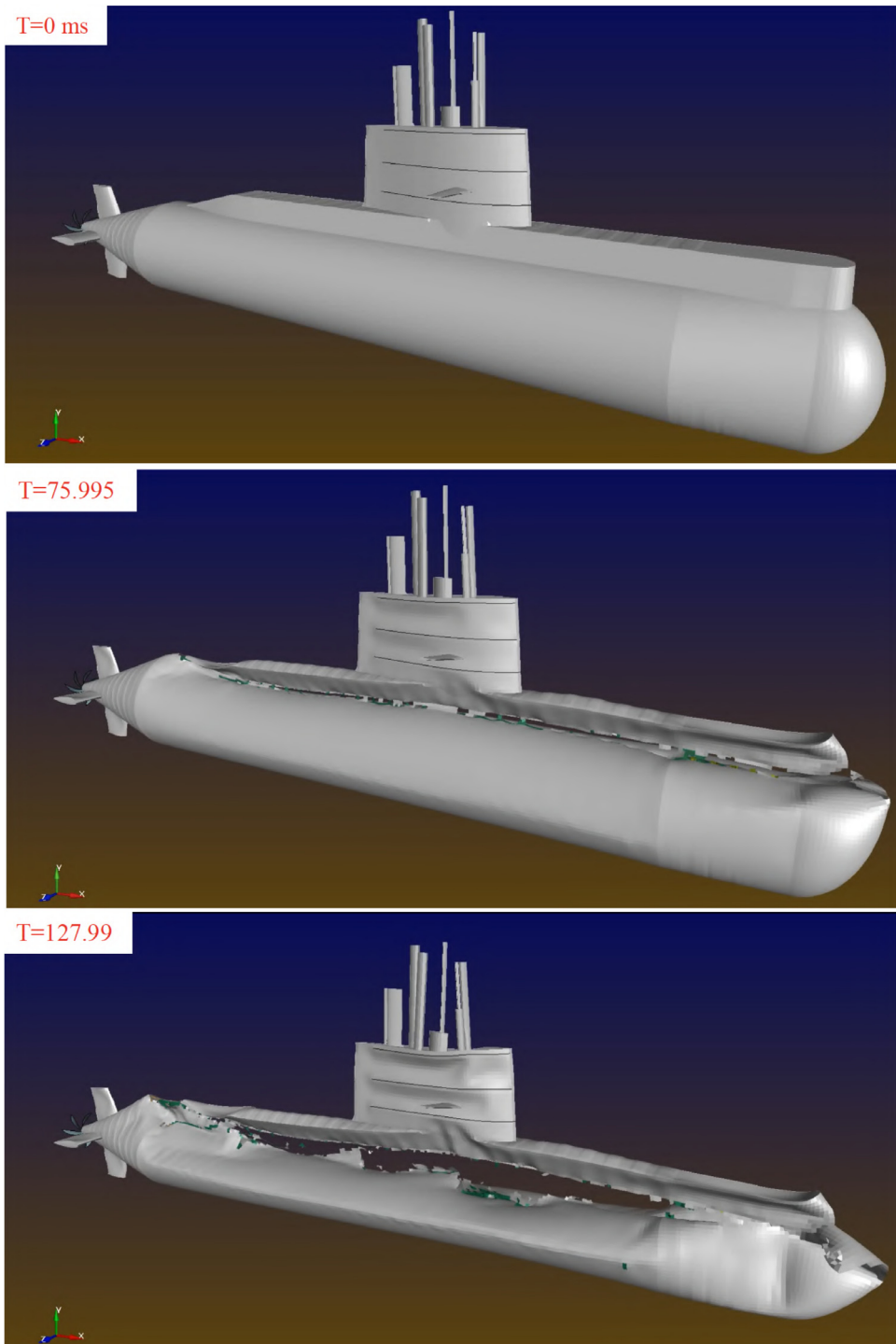


**Fig. 19.** An animation sequence of the submarine implosion with ring-stiffeners and stringers inside. For video animation, see: [https://1drv.ms/v/s!Alu8\\_wrOtHEkhA09nDTQ2MghP91U?e=4T3ofg](https://1drv.ms/v/s!Alu8_wrOtHEkhA09nDTQ2MghP91U?e=4T3ofg).

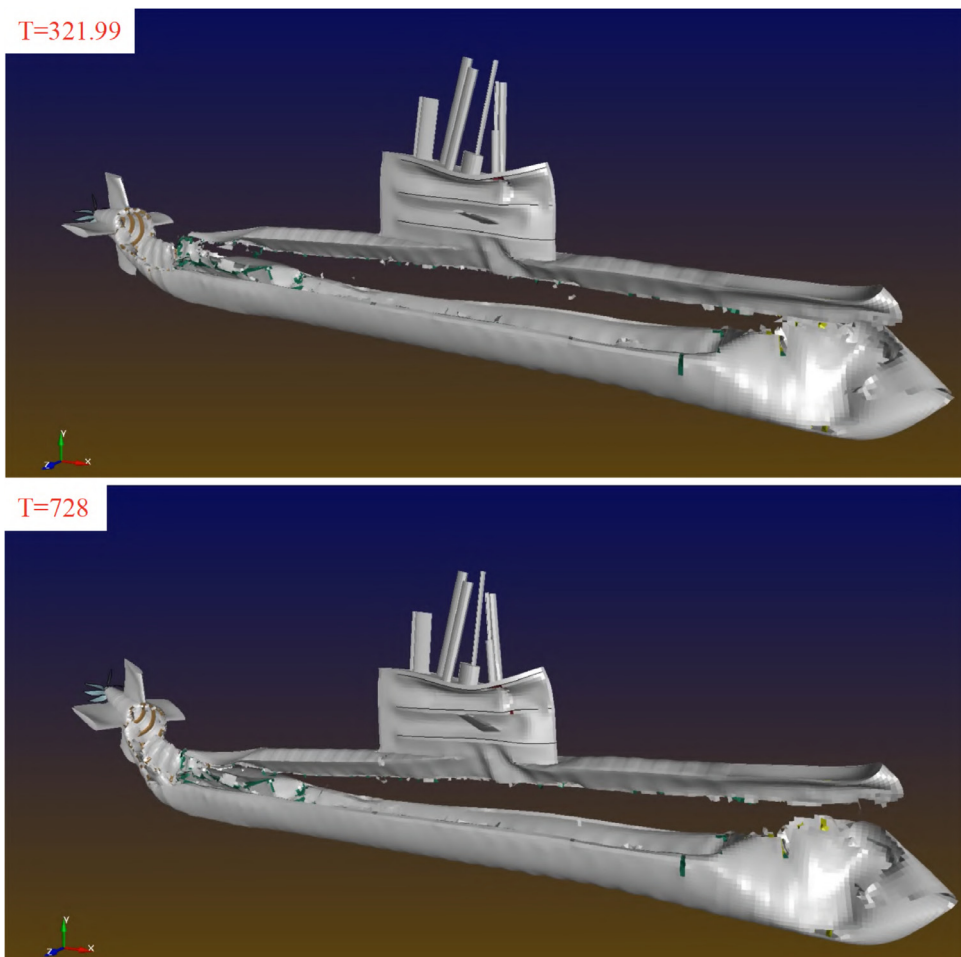


**Fig. 19.** Continued

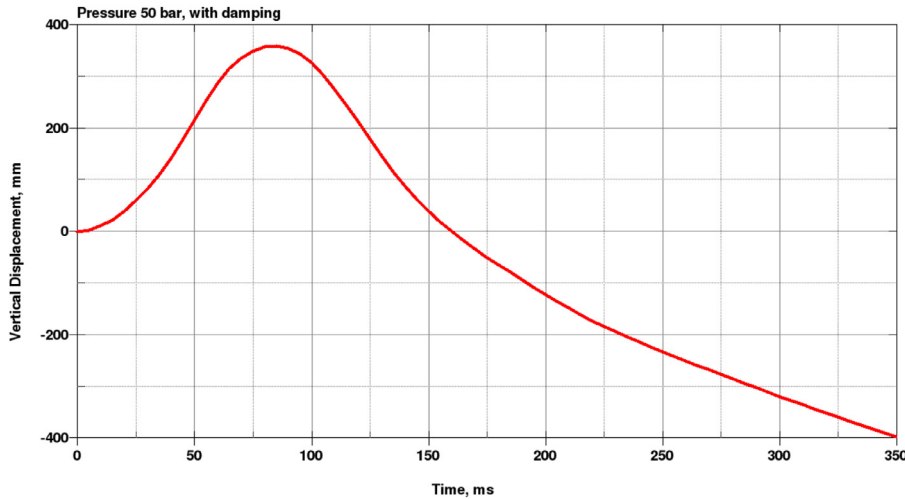


**Fig. 20.** The trajectory of the center of mass of an imploded submarine corresponding to the event in Fig. 23.

This video animation represents the *centerpiece* of the work on visualization in this paper and we recommend it as a must-see for the interested reader.

As a main conclusion of this subsection, computationally we have shown that the installation of ring-stiffeners can definitely improve the capability of a submarine to withstand larger undersea water pressure and defer implosion.

**Remark 2.** Even though the primary objective of this paper is just to conduct plain, faithful simulations, in the process of carrying out the computational work, we have found an interesting physical phenomenon, namely, in a submarine implosion process, at the beginning, the center of mass of the imploded submarine goes up at first, as can be seen from Fig. 20. This is surprising because one may tend to think that the center of mass is going straight down as the submarine is sinking. The paper by Lin and Liao [39] might offer some initial clue to the investigation of this phenomenon.

**Remark 3.** As a submarine malfunctions and is sinking, it may not be able to hold its regular balanced, cruising position as shown in the top panel of Fig. 23. The submarine may sink in a tilted head-down-tail-up attitude, or fall sideways. Such different possible configurations have been shown in another animation by Kostack studio [40]. Here, we display two such cases in Figs. 21 and 22.

**Remark 4.** In comparison among the four sets of graphics in Figs. 15, 19, 21 and 22, we have found, through visual inspections, that the patterns and damages of Figs. 19 and 21 are similar, while those of Figs. 15 and 22 are notably different, indicating that symmetry, attitudes and structural support play an important factor in the assessment of patterns and damages to a submarine in an implosion event.

In addition, Remark 1 (in Section 3.1.1) remains valid, namely, in a submarine implosion, regardless of the submarine's attitudes, fissure openings first tend to happen along ridges and edges of the hull of a submarine. Therefore, corners and edges should be rounded out as much as possible, which should have the beneficial effects of deferring and deterring implosion.

#### 4.3. The pressure impulses of a submarine implosion

We are able to capture the pressure impulse signal at a few sensor points and show a sample signal in Fig. 23.

For any computation of this sort, it is best that the sensor locations be placed *at a large distance, say a few hundred kilometers, away from the submarine*. Thus, it would seem to require an extremely large computational domain. However, this may be somehow avoided by assuming a *non-reflecting boundary condition*, which is available in LS-DYNA by the keyword \*BOUNDARY\_NON\_REFLECTING. For example, our computation in Fig. 12 was done by adopting this feature (which is easy because the initial pressure in the pressurizing water tank is nearly uniform around the test cylinder). However, we have difficulty adopting non-reflecting boundary conditions for the submarine cases for the reason that the submarine's size is not small so the water pressure around it is not initially near a constant.

We believe that this situation can be improved in the future so we can compute submarine implosions with a non-reflecting boundary condition and obtain much better implosion impulse signals.

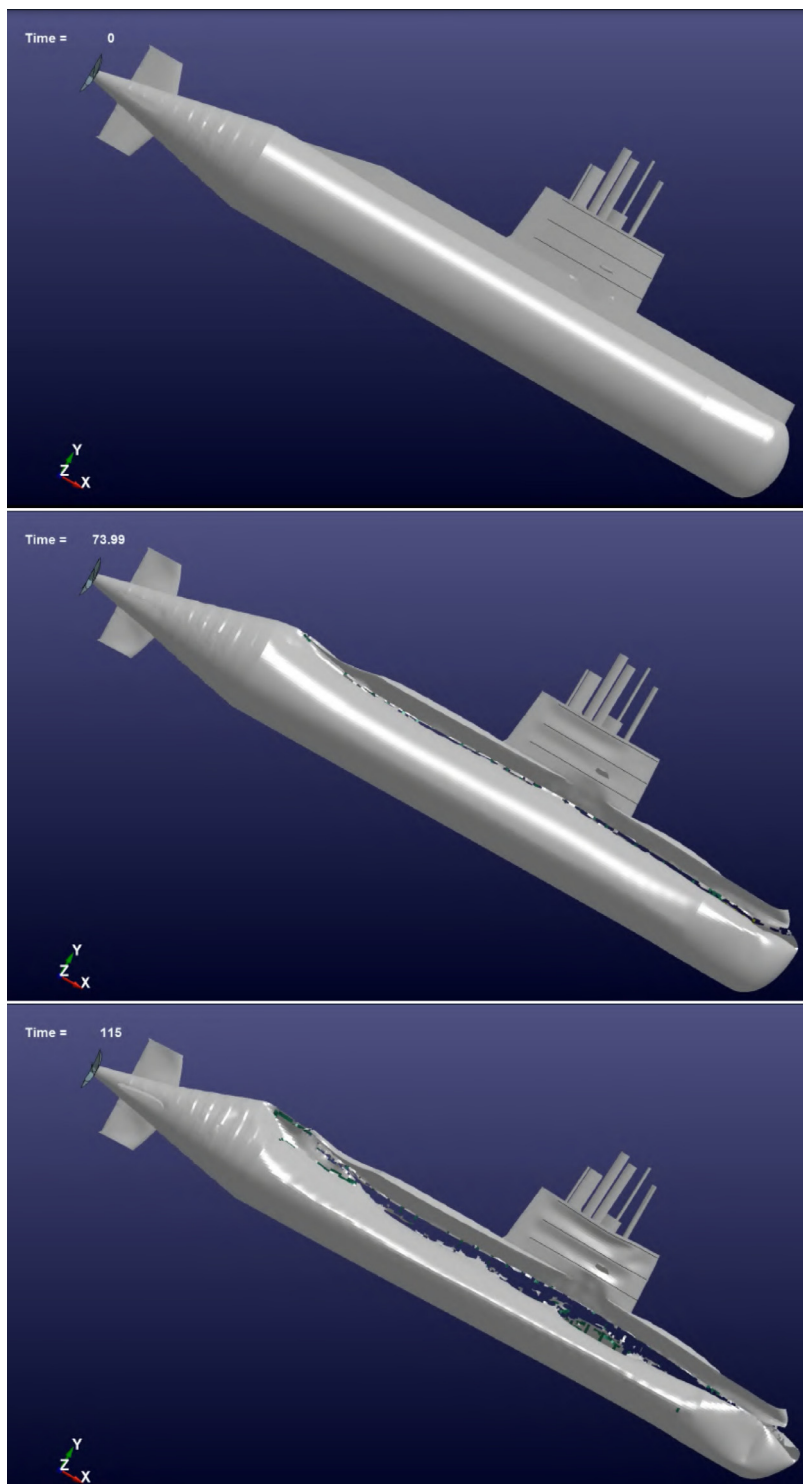


**Fig. 21.** Implosion dynamic sequence of a submarine from an initial “tilted position”. All the other conditions such as water depth and pressure are similar to those in Fig. 19. For the video animation, see [https://1drv.ms/v/s!Alu8\\_wrOtHEkhDYvpMmW944ukHHD?e=go7UHZ](https://1drv.ms/v/s!Alu8_wrOtHEkhDYvpMmW944ukHHD?e=go7UHZ).

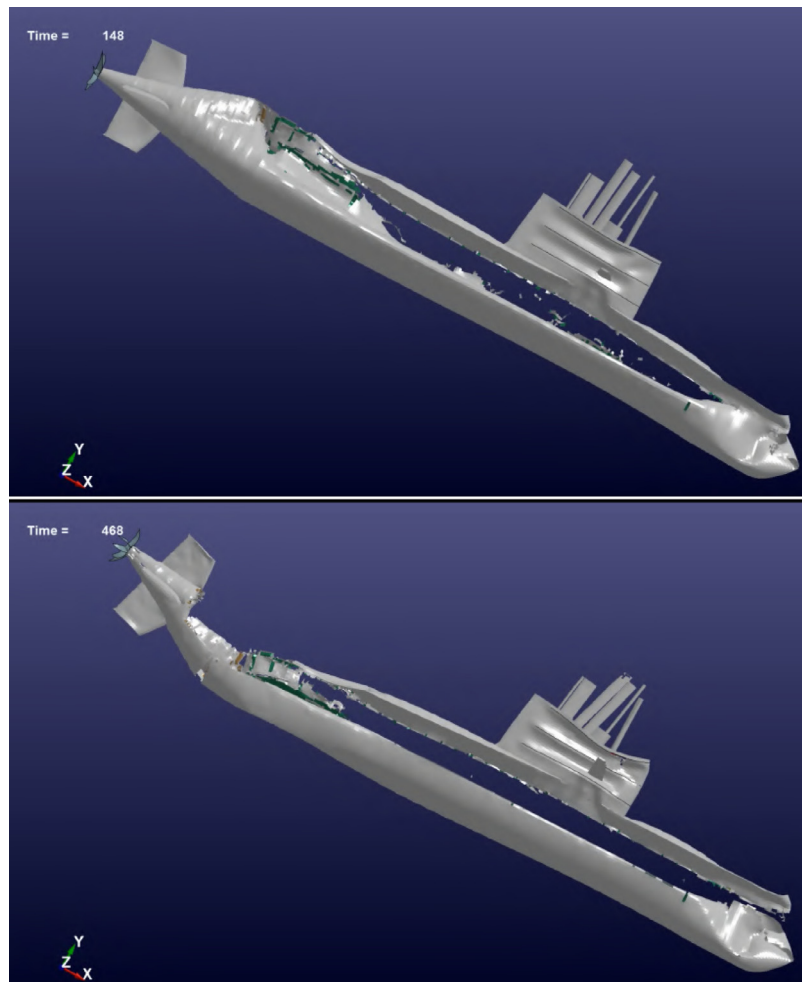


**Fig. 21.** Continued

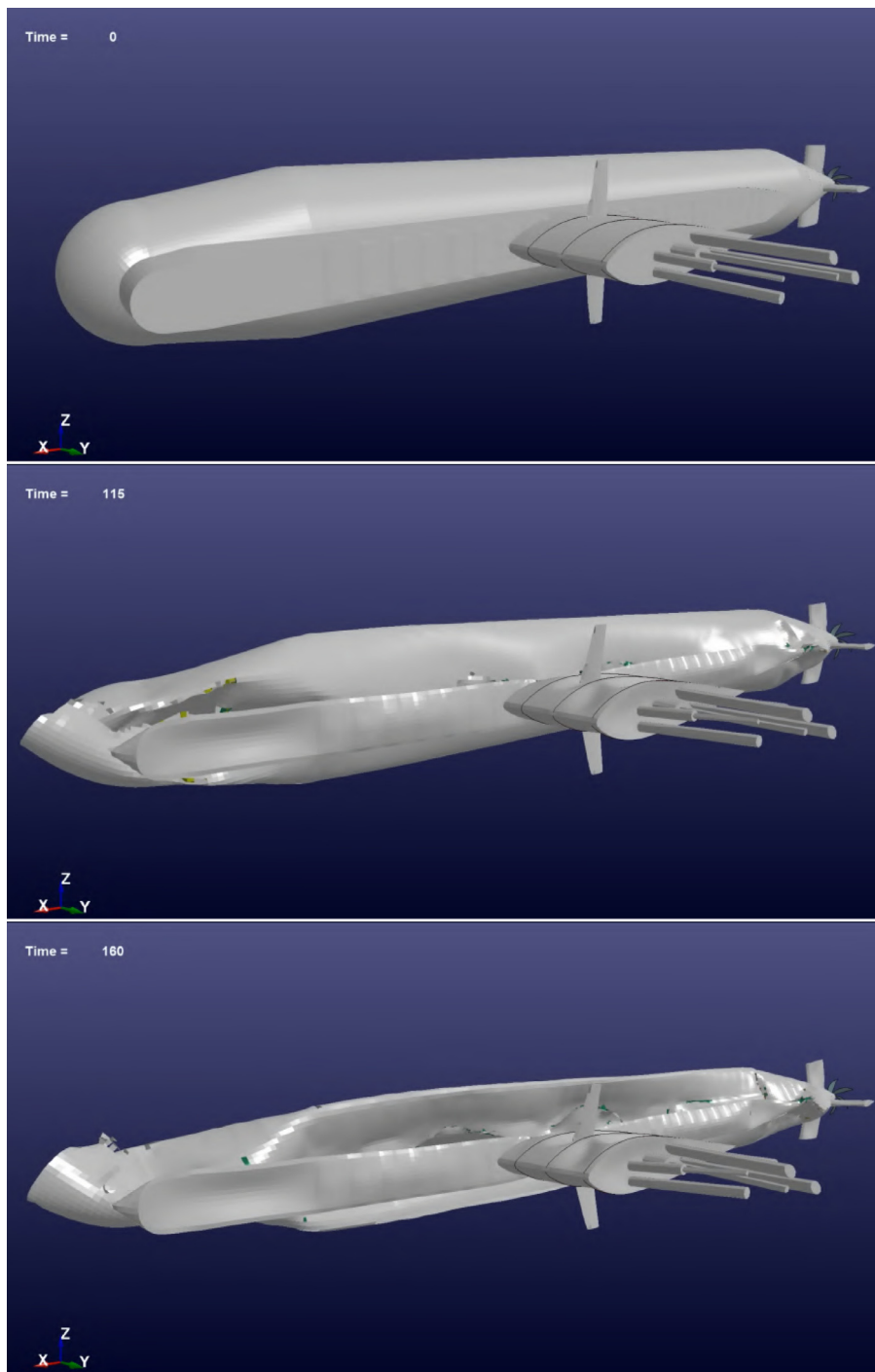


**Fig. 22.** Implosion dynamic sequence of a submarine listed in 90° in an initial “sinking sideway” position. All the other conditions such as water depth and pressure are similar to those in Figs. 19 and 21. For the video animation, see [https://1drv.ms/v/s!Alu8\\_wrOtHEkhDeUZTWuAw75ZquJ?e=MMUTGe](https://1drv.ms/v/s!Alu8_wrOtHEkhDeUZTWuAw75ZquJ?e=MMUTGe).

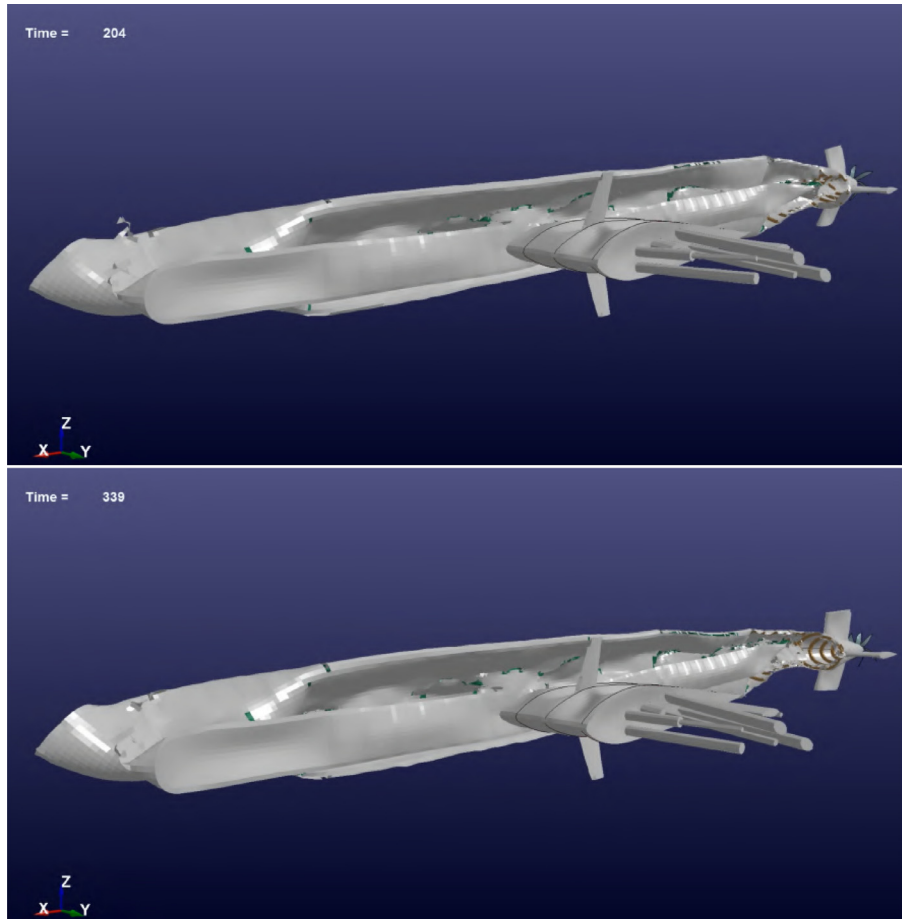


**Fig. 22.** Continued

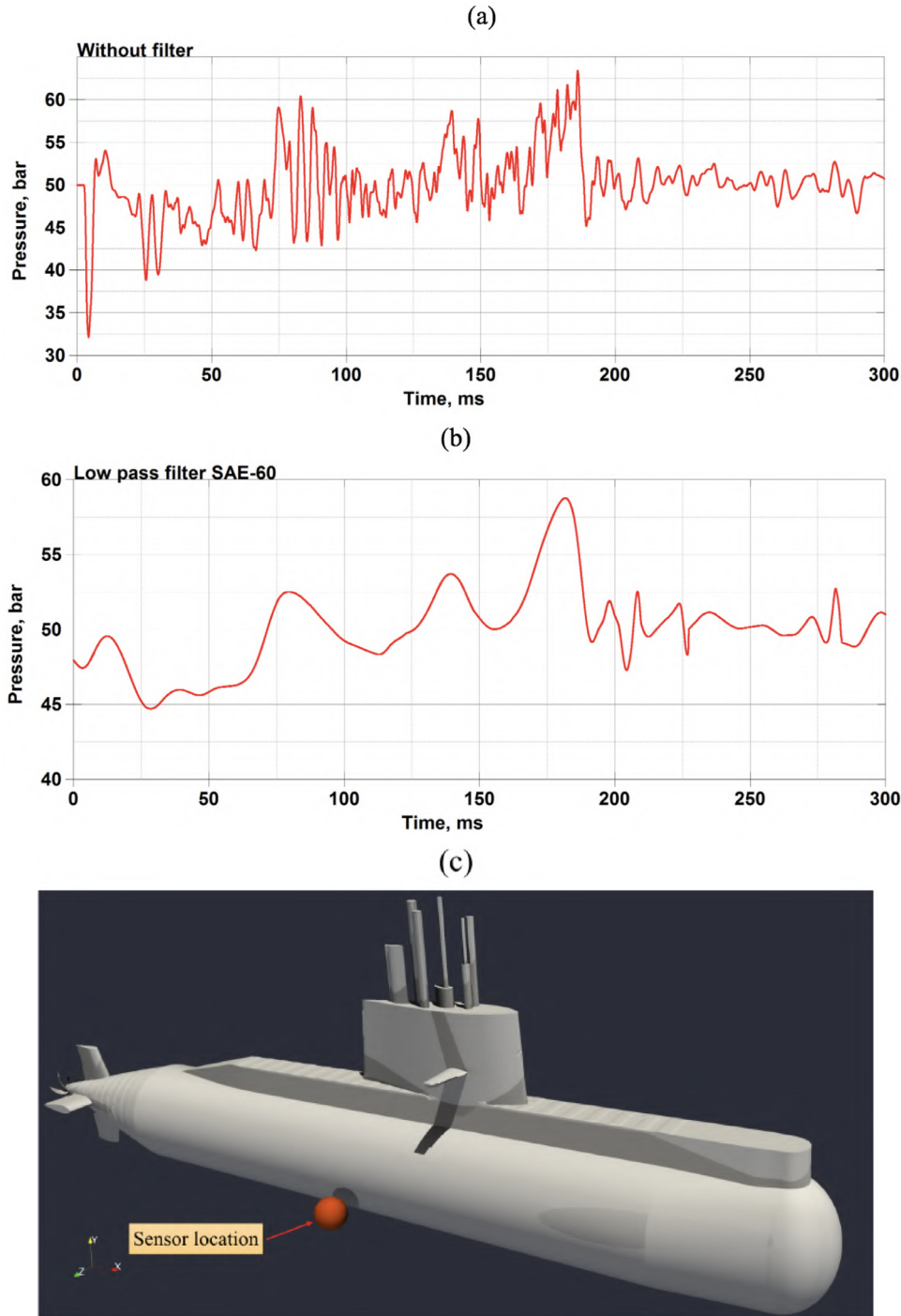


**Fig. 23.** The top panel (a) shows the computed pressure impulse signal at sensor location (40000, 0, 8000), which is indicated in panel (c). This is filtered to eliminate high frequencies, which is then shown in panel (b). It appears that the signal in (b) consists of several sub-implosions. The tail positions in both signals (a) and (b) are mainly reverberation from computing domain boundary reflections and, therefore, should be disregarded.

*Note:* The sensor is fixed in space with coordinates (4000, 0, 8000) in the unit of mm. The origin of reference is the submarine's center of gravity, located approximately at the point (4000, 0, 0) with an approximate main hull radius of 4000 mm. (The distance between the sensor and the hull is about 4 m.).

## 5. Comparisons between our supercomputer simulations and movie-style artistic rendering

Because the differences of methodologies between our work here (cf. Section 4.2) and movie-making [20] are fundamental, we naturally expect that differences of the manifested effects between the two are numerous. Here, we list eight sets of them in Figs. 24–31, by providing graphics side-by-side with comments. “Ratings” are given in Table 2.

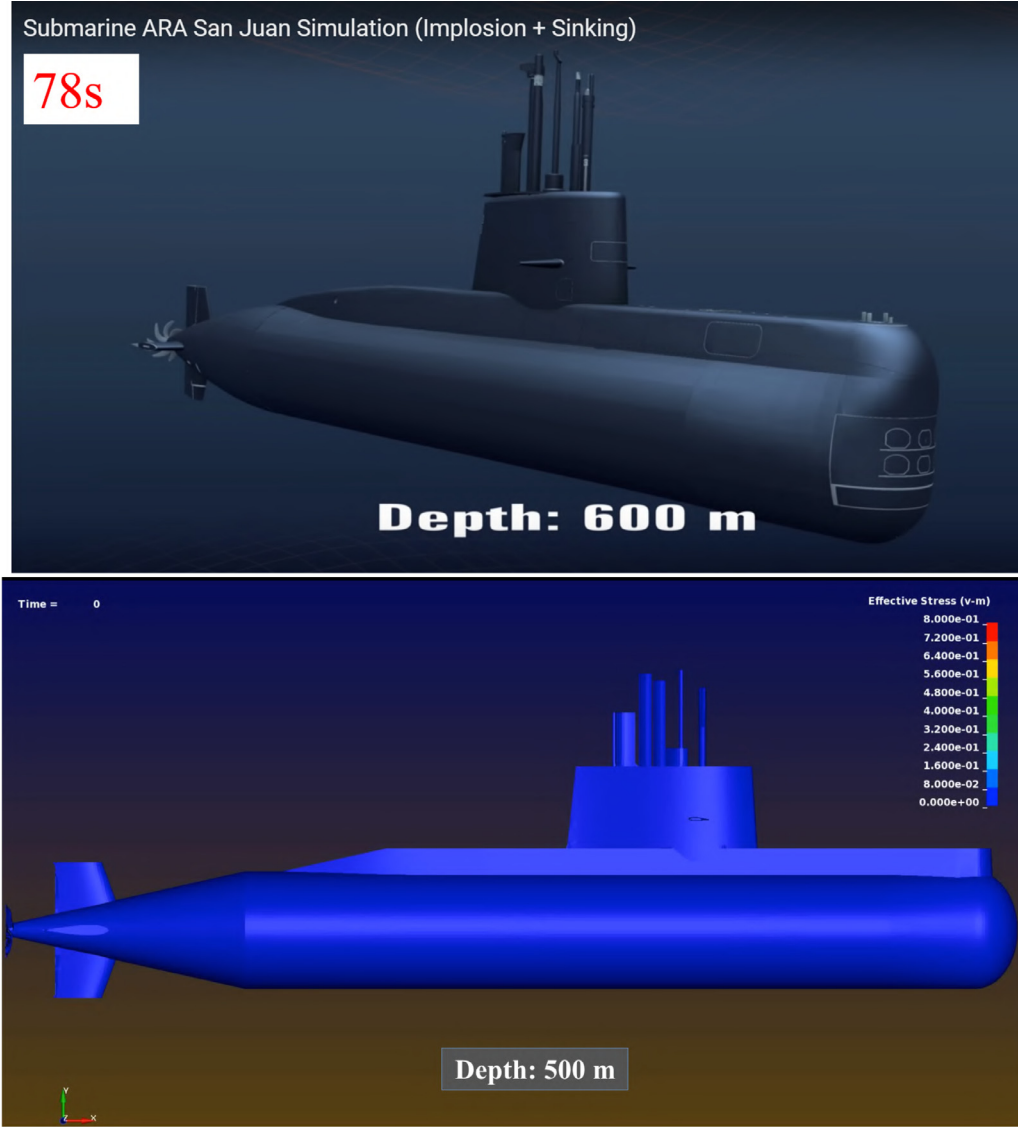


**Fig. 24.** Movie [19] assumed or used the water depth as 600 m, upper panel. Our computation shows that implosion happens at depth 500 m (or possibly somewhat even shallower).

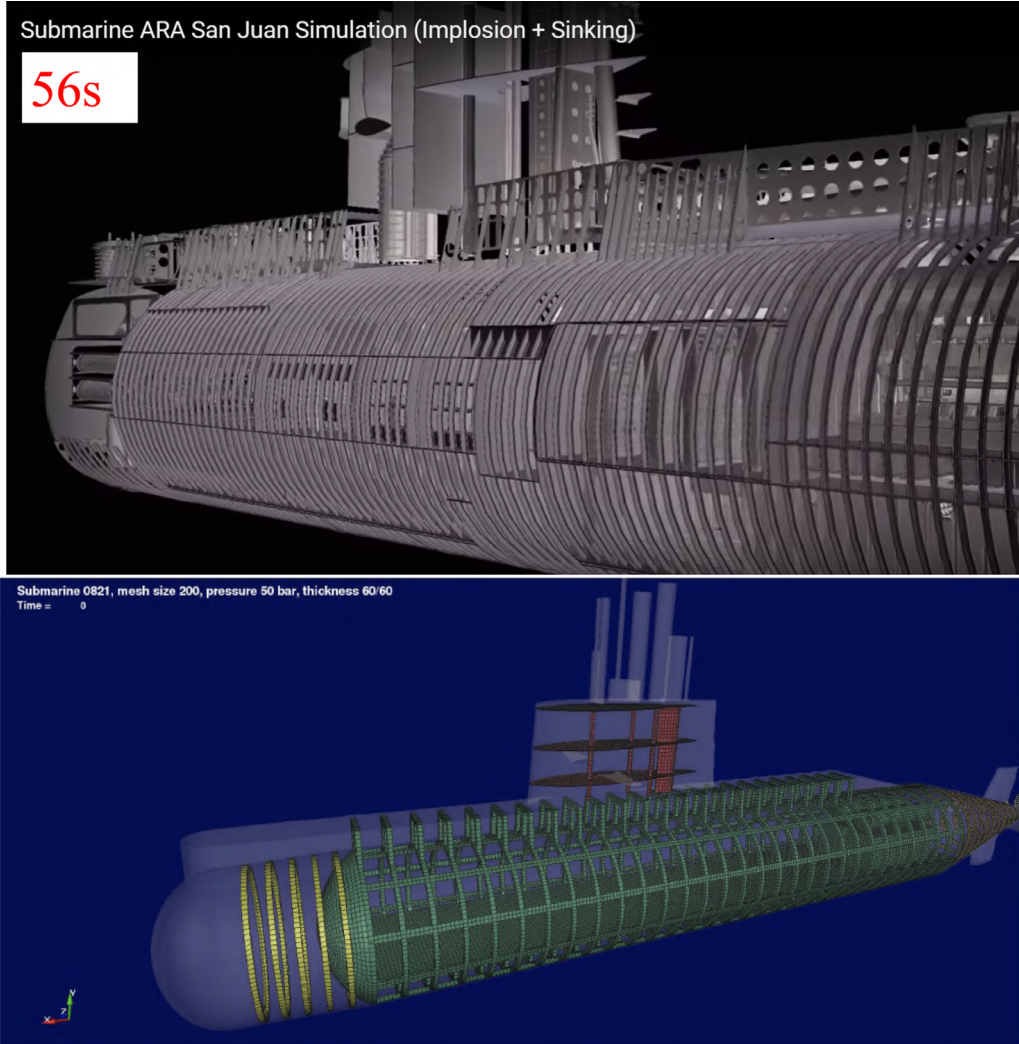


**Fig. 25.** Movie [19] is able to include many internal structures and furnishings inside the submarine, upper panel. The submarine in our work, due to limitation of supercomputer storage, has mainly the ring-stiffeners and supporting structures in place but otherwise has nearly an empty interior (see more in Fig. 29).

**Table 2**

This is a tabulated summary based upon the comparative graphics in Figs. 24–31 between the Hollywood-style movie [19] and our computational mechanics work. Each item is rated with a “+” or “−”, with the item of “Stress” doubly weighted, as it represents the most important value here in the sense of design and safety. These ratings also show deficiencies in the visualizations of both computational mechanics and Hollywood-style movie-making which could be further improved in the future.

Features	Artistically rendered movie [19]	Rating	Computational mechanics	Rating
Stress	Unavailable	− −	Yes; cf. Figs. 26 and 27	++
Fracture and break up	Yes, but patterns deviate from reality; cf. Figs. 26–28. In addition, very little bending and twisting are seen.	−	Shown; cf. Figs. 26, 27, 28, 30 and 31	+
Air bubbles leakage and rise	Yes; cf. Figs. 26 and 27	+	Unavailable	−
Interior layout	More complete; cf. Figs. 25 and 29	+	Incomplete	−
Water depth of implosion	600 m; cf. Fig. 24		500 m; cf. Fig. 24	
Crush pattern	Vertically downward; cf. Fig. 30	−	Concentrically inward; cf. Fig. 30	+
Cabin flooding	Unavailable; cf. Fig. 30	−	Unavailable; cf. Fig. 30	−
Final resting on seabed	Yes; cf. Fig. 31	+	Not shown	−
Summary	Three pluses (+), five minuses (−)		Four pluses (+), four minuses (−)	

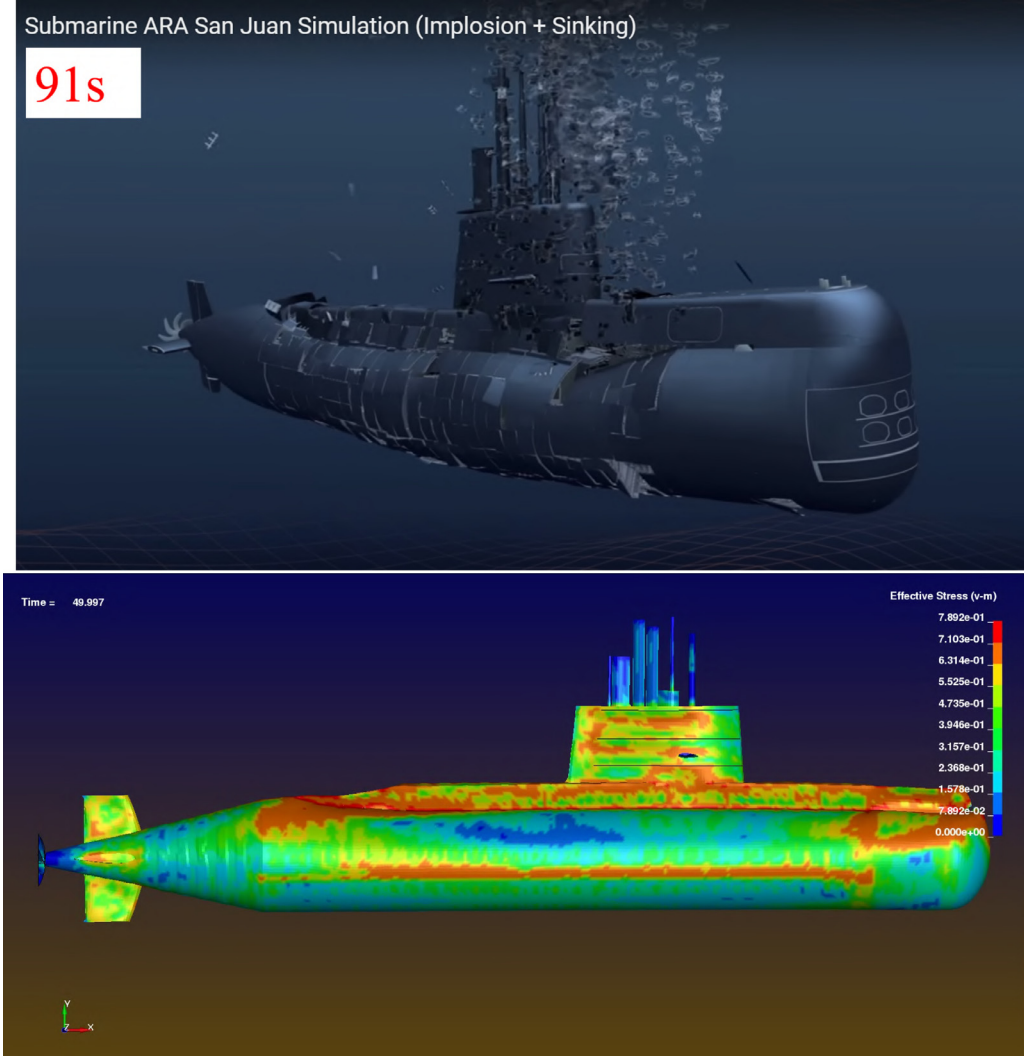


**Fig. 26.** The upper panel, from movie [19], shows one of the initial instants when implosion happens. The main body of the submarine is already fracturing, and many large air bubbles are leaking out and rising. However, it is not possible to know the magnitude of stress exerting on the submarine. In our work, lower panel, initially when the implosion happens, we can see the stress (force) field intensity on the submarine, represented in color. The whole submarine is getting crushed, with the most severe weakening of structure at the rim of the superstructure of the submarine. Nevertheless, we are not able so far to show the leaking and rising air bubbles.

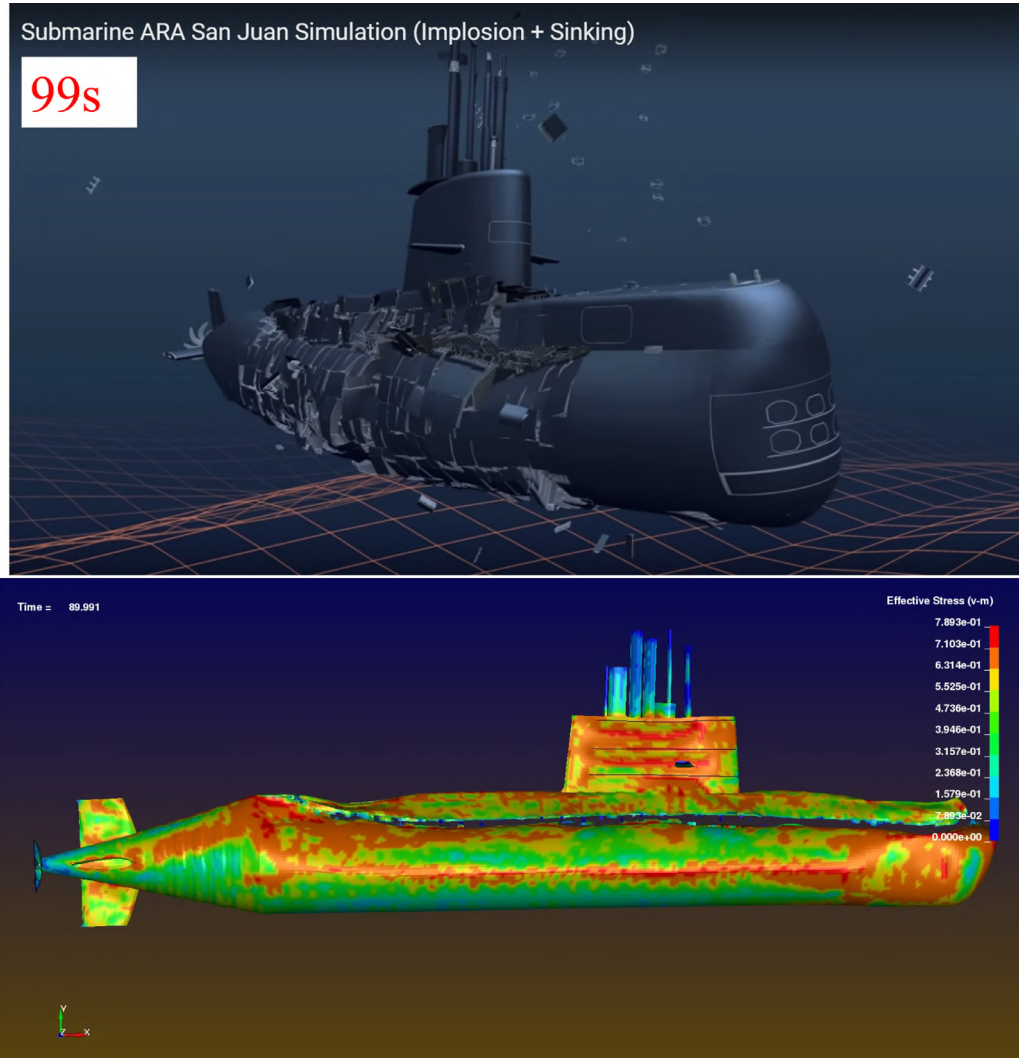


**Fig. 27.** The upper panel (from movie [19]) and lower (from our work) panel show distinctive structural collapse and fracturing patterns. Especially, note that the conning tower of the submarine in the upper panel has not suffered much deformation. This is questionable and unlikely.

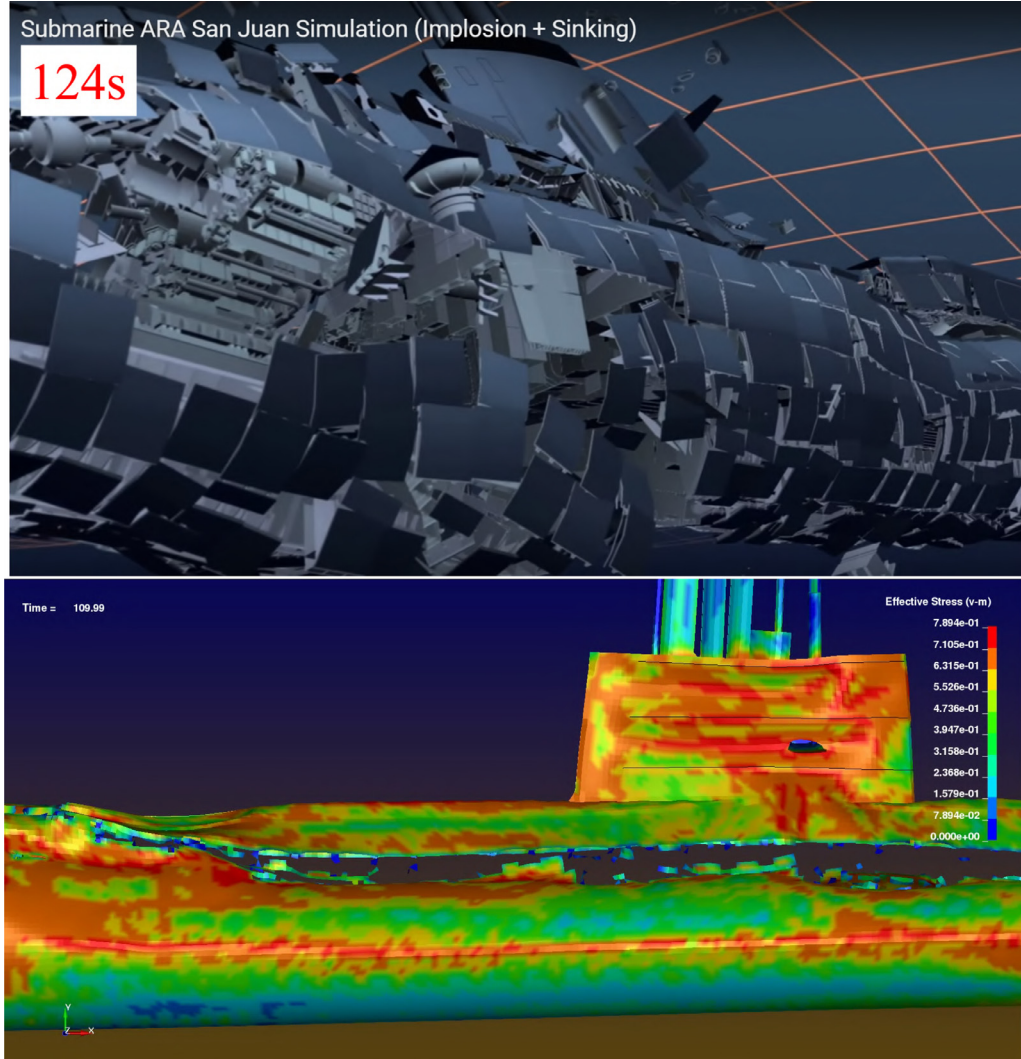


**Fig. 28.** The metal hull of the submarine in the upper panel (from movie [19]) breaks up largely in rectangular pieces. This is an artificial effect. Our work, lower panel, shows the fracturing, bending and twisting of the metal hull in a totally different way.

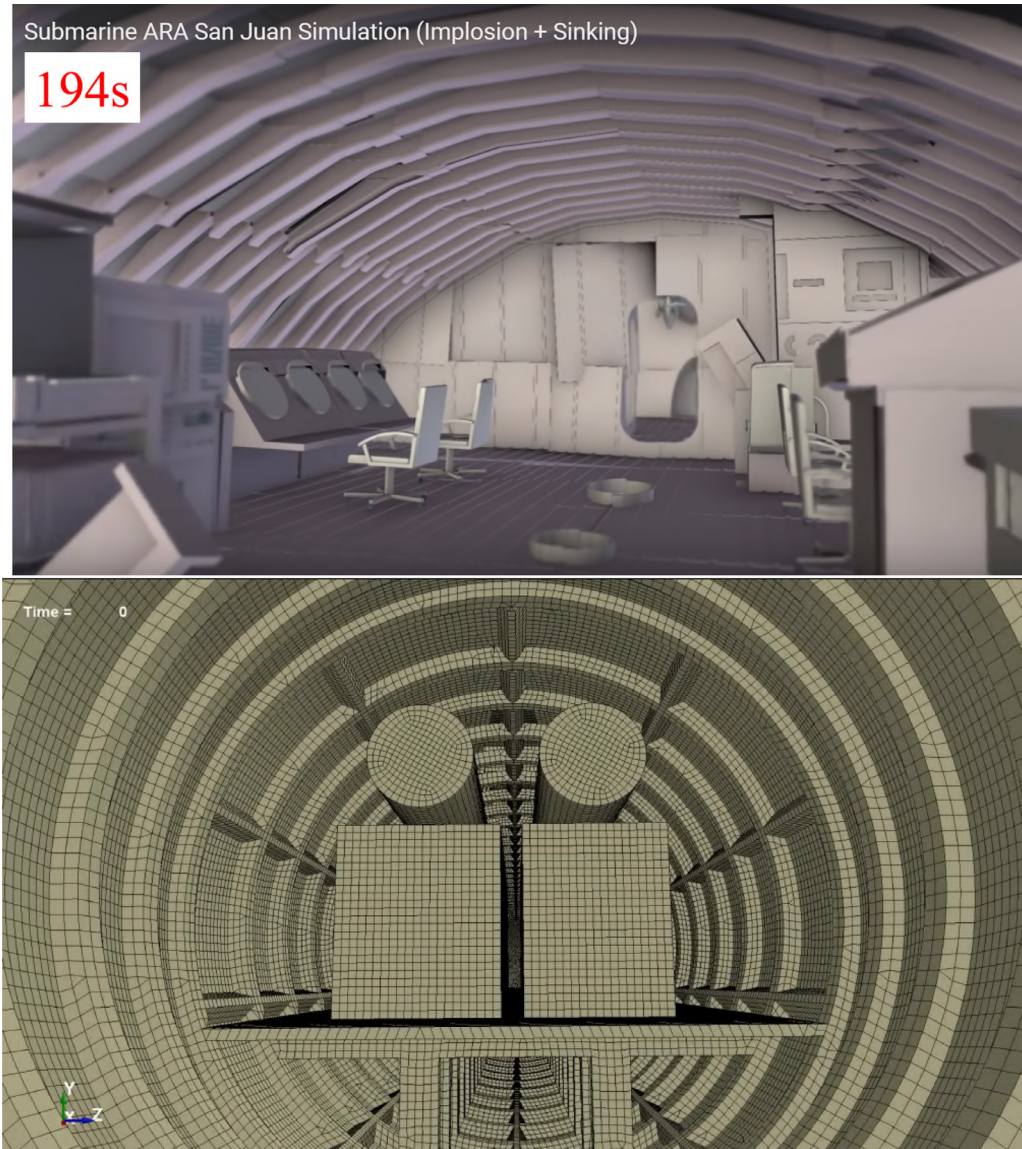


**Fig. 29.** The upper panel from movie [19] displays more internal furnishings than that in our work (where only two cubic boxes and two spherical containers, all hollow, are displayed). Neither panels seem to have modeled the submarine's internal parts correctly, because it is well known that the interior of a submarine is generally quite huddled.

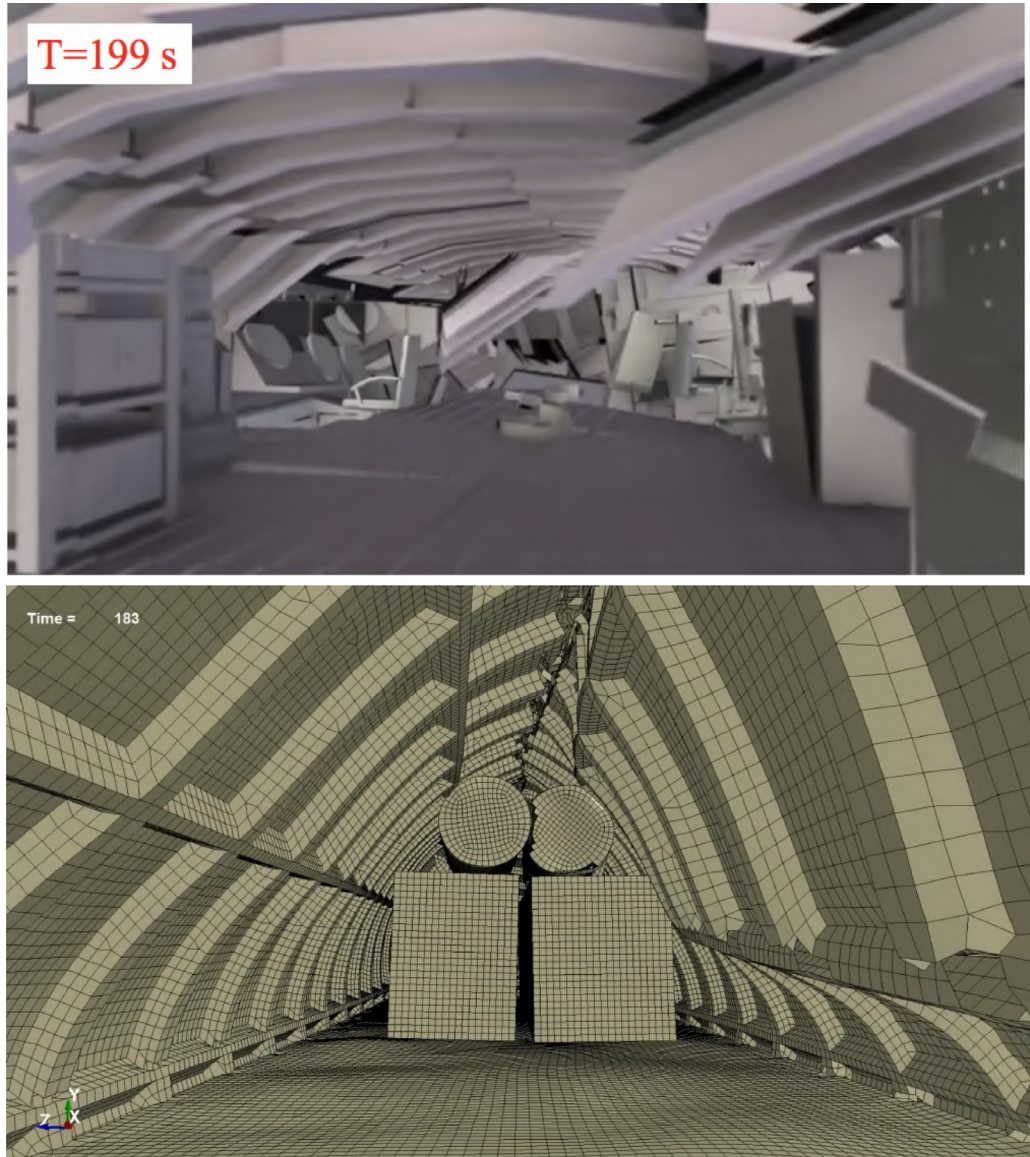


**Fig. 30.** The upper panel from movie [19] shows that the ceiling in the interior of the submarine is crashing down from the top, while our work (lower panel) shows that the interior of the submarine is squashed somewhat *inward*. Neither of the two panels show the flooding of water rushing into the submarine cabin because of the openings of fissures.

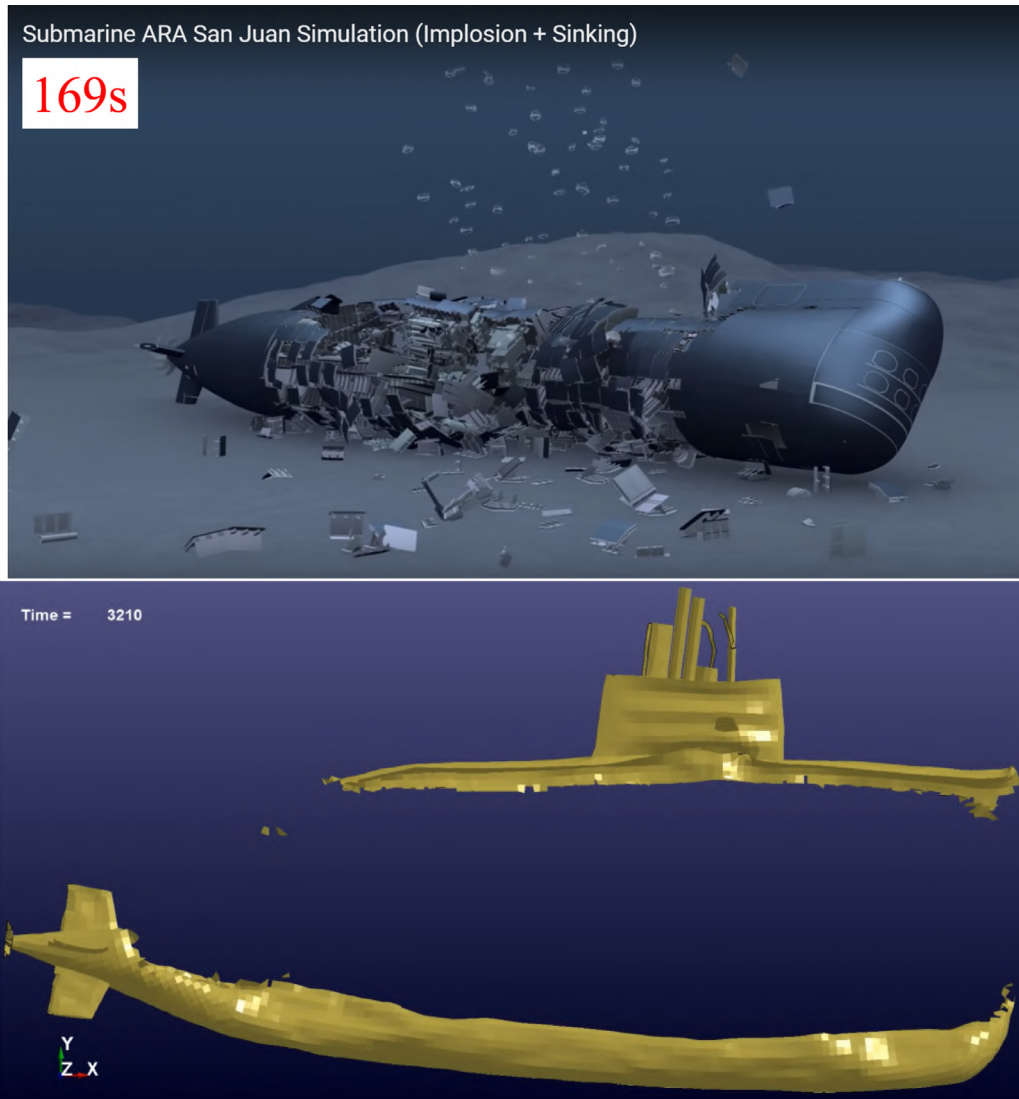


**Fig. 31.** The upper panel shows that, at the end of movie [19], the submarine comes to rest on the ocean floor. We are not able to show this in our work, lower panel, due to possibly much longer supercomputer time and the needs of some significant additional programming.

## 6. Concluding remarks

Only a tiny number of people have been able to see large-scale transportation disasters such as the crash of airplanes or the collision of ships actually *taking place in situ*. But (virtually) nobody has been able to witness the occurrence of a submarine implosion because it happens in dark, deep water. Our work here should help the *visualization and realism* of, say, the movie-making of underwater implosion.

One of the aims of this paper is to perform *event reconstruction* for the contemporary problem of underwater implosion of the Argentinian submarine ARA San Juan S-42. Such event reconstructions are useful for *legal forensics* purposes in court proceedings. However, our objectives are not only limited to forensic analysis - we are actually more interested in the acquisition of knowledge for the future underwater structures and vehicles so that improvements of their *structural integrity and safety* can be made (cf. Remark 4). Thus, this paper is similar in nature and spirit to the earlier publications [41] and [21] on the simulations and visualization of the air crashes of Malaysia Airlines flight MH370 and German Wings flight 9525 by the research team of Dr. Goong Chen at the Math. Dept. of Texas A&M University.

The approach taken by us in this paper is based on *FSI, the fluid-structural-interaction approach* taken in a more straightforward way via computational mechanics and modeling than the earlier studies, as nearly all of our PDE solvers were taken directly from the software LS-DYNA. (In contrast, authors of the earlier papers in this field mostly have to develop their own computer codes.) Furthermore, our models have incorporated fracture effects, which were not featured in the computational work done earlier by other groups.

The above notwithstanding, due to our limited computer and human resources, the computer model constructed for the submarine (cf. Figs. 14, 16 and 17) under treatment is still crude. Furthermore, for a large scale scientific computation project like this one, in order to achieve higher accuracy, finer meshes are definitely needed but not attained by us here because of the limitation of supercomputer storage - our computational domain is quite small. There remain many other open questions regarding underwater implosion which require dedicated attention. We include our LS-DYNA computer codes in Appendix C for public use and scrutiny. We hope that our paper and computer codes can stimulate and facilitate further interests and work in similar directions.

## Credit Author Statement

Chunqiu Wei: model building, supercomputing, code development, literature survey  
 Goong Chen: technical leadership, general direction and advisement, modeling, technical writing  
 Alexey Sergeev: supercomputing, code development, visualization  
 Jean Yeh: supercomputing, code development, visualization  
 Jianhua Chen: conceptualization, literature survey, modeling  
 Junmin Wang: conceptualization, literature survey, modeling  
 Shaochun Ji: conceptualization, literature survey, modeling  
 Jiao Wang: conceptualization, literature survey, modeling  
 Donghui Yang: conceptualization, literature survey, modeling, funding  
 Shuhuang Xiang: conceptualization, literature survey, modeling, funding  
 Xiaomin Cao: conceptualization, literature survey, modeling  
 Wenying Lu: conceptualization, literature survey, modeling  
 Marlan O. Scully: conceptualization, literature survey, modeling, funding

## Declaration of Competing Interest

The authors declare that they have no known competing financial interests or personal relationships that could have appeared to influence the work reported in this paper.

## Acknowledgement

C. Wei was supported by the Chinese Scholarship Council for 2-year study at Texas A&M University by grant #201706030045. G. Chen, J. Yeh and A. Sergeev were supported in part by Qatar National Research Fund grant #NPRP9-166-1-031. J. Yeh was partially supported by Taiwan's National Science Council grant NSC 108-2115-M-017-005-MY2. J. Chen was supported by the Chinese Scholarship Council grant #201708430032. Junmin Wang was supported in part by NSFC grant #[61673061](#). S. Ji was supported in part by Qing Lan Project of Jiangsu Province. Jiao Wang was supported by the Chinese Scholarship Council for 1-year study at Texas A&M University by grant #201806030080. D. Yang was supported in part by NSFC grant #[11871478](#). S. Xiang was supported in part by NSFC grant #[11771454](#). X. Cao was supported in part by NSFC grant #[11671240](#) and [11871315](#). W. Lu were supported by the Chinese Scholarship Council grant #201709480014. Marlan O. Scully was partially supported by the Office of Naval Research (Award #[N00014-20-1-2184](#)), the Air Force Office of Scientific Research (Award #[FA9550-18-1-0141](#)), the Robert A. Welch Foundation (Grant #A-1261) and King Abdulaziz City for Science and Technology (KACST). All coauthors wish to thank Texas A&M Universitys High Performance Research Computing Center for technical assistance and for generous allocation of hours.

## Appendix A. ALE, FSI, and Pressure Loading

### A1. Fluid-structure interactions (FSI)

With the ALE solver, the FSI problems studied by LS-DYNA, the fluids are modeled with ALE hexahedrons and the structure is modeled with Lagrangian shells or solids. In such a model, the Lagrangian mesh usually does not share nodes with the ALE mesh. Rather, the two meshes interact via a coupling algorithm defined with the command \*CONSTRAINED\_LAGRANGE\_IN\_SOLID. This coupling serves to generate forces that resist penetration of the ALE material through the Lagrangian parts. Coupling is a key and sometimes complex aspect of ALE modeling. (Please see the specific keywords in [Appendix C](#).)

### A2. Loading of pressure

#### A2.1. 'Dry' model

In the 'dry' model, we load pressure to the cylindrically-shaped shell tube by using the keyword \*LOAD\_SHELL\_SET\_ID.

#### A2.2. Modeling with water and air

In a model with water and air, an initial pressure field in one or more of the ALE materials is known, e.g., atmospheric pressure in air or hydrostatic pressure in water. However, the case is more complex where pressure varies with depth as in the case of water. The command \*INITIAL\_HYDROSTATIC\_ALE can be used as an aid to greatly reduce the time it takes to initialize the hydrostatic pressure and reach a steady state condition in the fluid. \*INITIAL\_HYDROSTATIC\_ALE, in conjunction with \*LOAD\_BODY, which applies gravity loading, and \*BOUNDARY\_SPC, which applies the normal direction constraints to the boundary, serves to quickly initialize the hydrostatic state of the fluids.

In addition, water has a large bulk modulus leading to high incompressibility. A small volume change will generate large pressure changes. This implies that large pressure oscillations may occur. We need to use damping to reduce the oscillations in pressure time histories. See [Appendix B](#) next. Furthermore, exterior segments must also have an applied pressure to equilibrate the internal pressure. Here we use \*CONTROL\_ALE to set the boundary pressure.

## Appendix B. Damping to Reduce Parasite Oscillations

"Parasite Oscillations" are known to happen in CFD computations. We first cite an elegant example, from Tam [42], as shown in [Fig. B.1](#). The best way to eliminate such oscillations is through numerical damping.

There are a number of numerical damping models available in LS-DYNA (cf. [43]), for example:

```
*DAMPING_FREQUENCY_RANGE
*DAMPING_FREQUENCY_RANGE_DEFORM
*DAMPING_GLOBAL
*DAMPING_PART_MASS
*DAMPING_RELATIVE
```

We have tested the effectiveness of numerical damping given above. What we have found is that \*DAMPING\_FREQUENCY\_RANGE is the right one for our choice.

\*DAMPING\_FREQUENCY\_RANGE is a frequency-independent damping option for a range of frequencies and a set of parts. This *proprietary* technique was developed by Richard Sturt and Yuli Huang of Arup Co. in U.K. It uses low amounts of damping only, e.g. usually up to 1% or 2%. The frequency range specified by the user should ideally be no more than a factor of 30 but in the newer version it can be increased to 100~200.

In our calculations of the validation case of the implosion of a test cylinder immersed in a pressured water tank (cf. [Section 3.2](#)), we can estimate the frequency range as follows:

For a low-order finite element method (such as the piecewise linear Lagrangian FEM), one needs 10 points per wavelength to resolve any spatial variation accurately. The associated frequency of a wave traveling at the speed of sound in water is [44]

$$c\lambda = (1500 \text{m/s})/(0.01 \text{m}) = 0.67 \times 10^{-5} \text{s}, \quad \text{where } \lambda = \text{wave length, cf. [44]}$$

or a resolvable frequency of 75 kHz (based on the Nyquist criterion). Please see some relevant info in [45, Chapter 13].

Assuming a CFL number of some fraction of unity and  $dx = 1 \text{ mm}$ ,  $dt$  should be less than roughly  $1 \times 10^{-6} \text{s}$  (in water). These qualifying numbers are all satisfied by LS-DYNA machine-selected  $dt$  and CFL.

We have tried a lowpass Butterworth filter with cutoff frequency of 75 kHz, and found that our earlier computed signal in [Fig. 12](#) remains essentially unchanged.

Hence, in our new computations on the supercomputer, we have set our frequency range to be the interval [5kHz, 1000kHz], with damping coefficient equal to 0.05. Please see the comparisons among the choices of damping coefficients: 0.00, 0.03, 0.05 and 0.08 in [Fig. B.2](#), and in [Table B.1](#).

In our computations of the submarine implosion, because of the size  $dx = 1 \text{ cm}$ , we have chosen the frequency range to be [15Hz, 3kHz]. The damping parameter remains the same as 0.05.

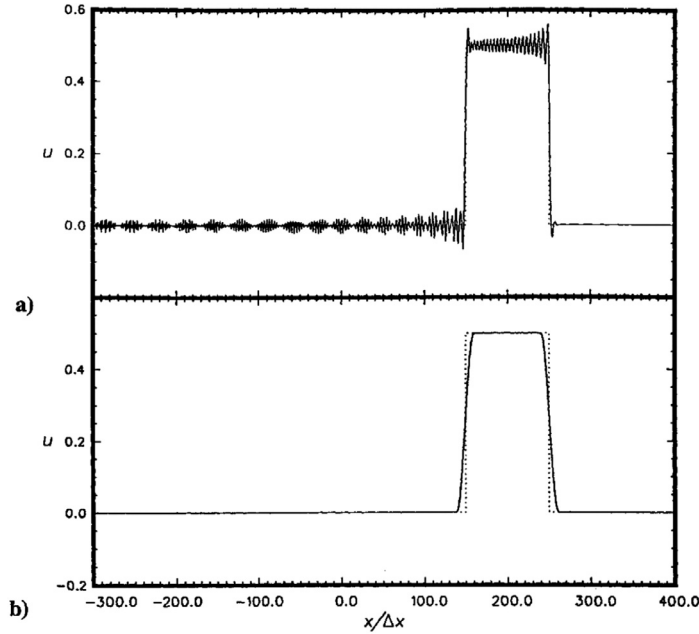


**Fig. 7** Waveform initiated by a disturbance with a box-car profile showing parasite waves and the effect of artificial selective damping:  
a) no artificial damping and b) with artificial damping.

**Fig. B.1.** (Excerpted from Tam [42]) Parasite oscillations as identified in the upper panel (a) of a simple CFD computation. Such oscillations can be and, in our revised work, have been eliminated by artificial damping.

**Table B.1**

Key values of  $P_{\min}$ ,  $P_{\max}$ ,  $\Delta T^-$ ,  $\Delta T^+$ , cf. Fig. B.2(a) for the comparison purpose.

	$P_{\min}$ (bar)	$\Delta T^-$ (ms)	$P_{\max}$ (bar)	$\Delta T^+$ (ms)	Error of $P_{\max}$
Experimental Farhat et al. [18]	-8.14	0.797	32.55	0.206	benchmark
Simulation Farhat et al. [18]	-8.97	0.694	28.2	0.323	-13.3%
No damping of our work	-10.74	0.708	40.87	0.165	25.5%
*DAMPING FREQUENCY RANGE (CDAMP=0.03)	-10.56	0.715	38.02	0.19	16.8%
*DAMPING FREQUENCY RANGE (CDAMP=0.05)	-10.46	0.76	35.95	0.205	10.4%
*DAMPING FREQUENCY RANGE (CDAMP=0.08)	-10.37	0.825	35.23	0.225	8.2%

Fig. 12 in Section 3 now has shown strong agreement and consistency with the experimental and computational results in Farhat et al. [18]. See Fig. B.2 and Table B.1. One can see a clear trend that the increase of damping parameters from 0 to 0.08 (8%) leads to decreased oscillations and a better match with the peak pressure. Thus, it is tempting that 0.08 is a better choice than 0.05. However, the discrepancies between the benchmark and the damping parameters 0.08 of  $\Delta T^-$  and  $\Delta T^+$  also grow. In addition, the design principle of \*DAMPING\_FREQUENCY\_RANGE by Sturt and Huang is that *this damping parameter should not be taken large*. Therefore, we settle with the choice of 0.05 rather than 0.08.

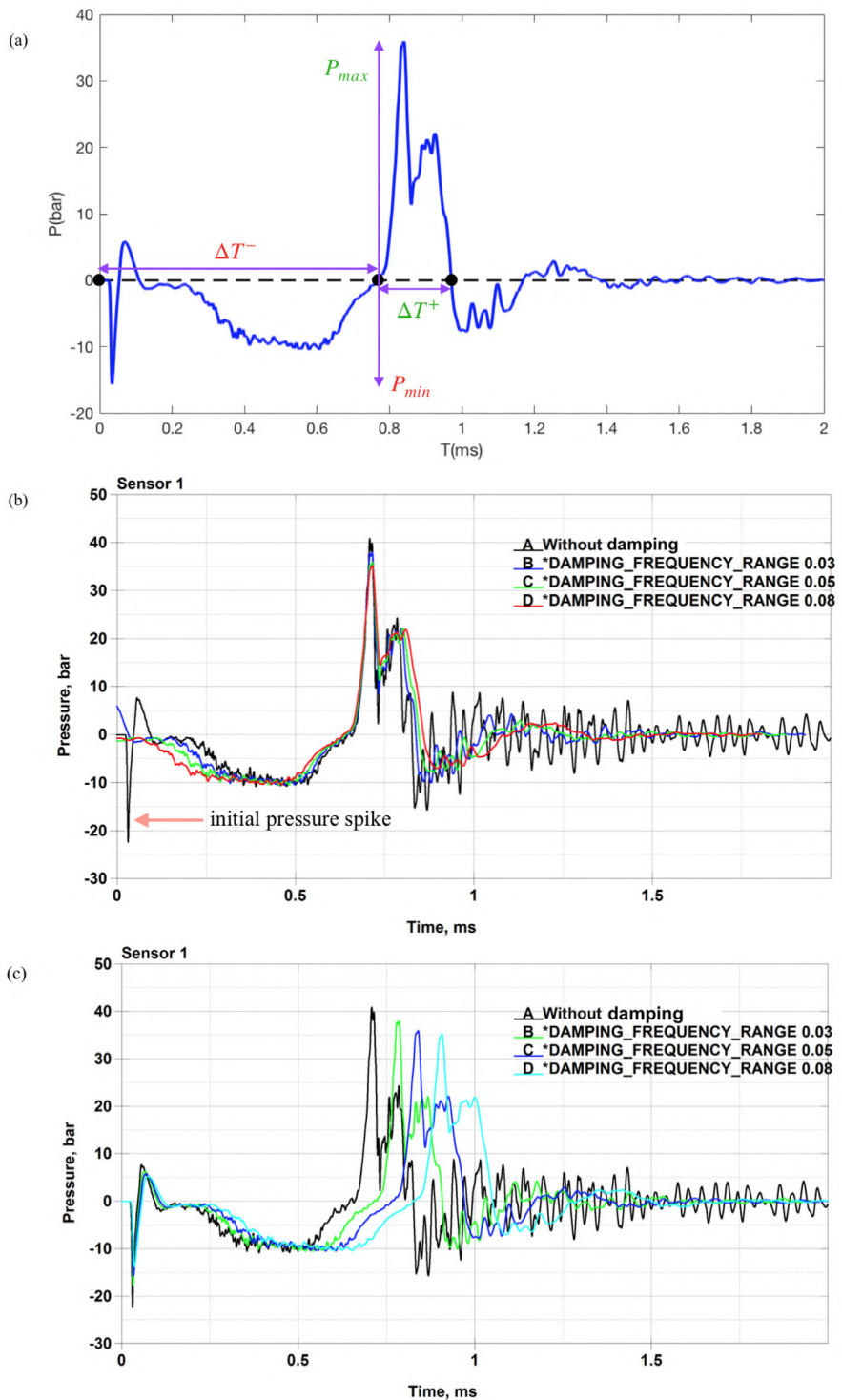


**Fig. B.2.** Comparisons among several choices of damping parameters: 0, 0.03, 0.05 and 0.08. (a) defining the various quantities to be used in Table B.1; (b) by overlaying highest peaks; (c) by same initialization time.

## Appendix C. LS-DYNA Computer Codes

### C1. Keywords for the 'Dry' model

```

*KEYWORD
*CONTROL_TERMINATION
$# endtim endcyc dtmin endeng endmas nosol
    0.8      0     0.0   0.01 .000000E8   0
$ Problem status report interval steps to the d3hsp file.
*DATABASE_GLSTAT
$# dt binary leur iopt
    0.1      0     0     1
$ Kinetic energy of lumped mass elements is output as kinetic
energy of part 0 in matsum
*DATABASE_MATSUM
$# dt binary leur iopt
    0.1      0     0     1
$ time interval of output
*DATABASE_BINARY_D3PLOT
$# dt lcdt beam npnltc psetid iopt
    0.005    0     0     0     0     0
$ restart settings of LS_DYNA
*DATABASE_BINARY_RUNRSF
$# cycl nr beam npnltc psetid
    1000.0   0     0     0     0
$ time-pressure curve output settings
*DEFINE_CURVE
$# lcid sidr sfa sfo offa offo dattyp lcint
    3       0   1.0   1.0   0.0   0.0   0     0
$# a1          o1
    0.0
    0.1   0.009
    1.0   0.01
$ impose pressure on tube by id
*LOAD_SHELL_SET_ID
$# id esid lcid sf at
    3       3     3     1.0   0.0
$ contact settings between plug and tube
*CONTACT_TIED_SURFACE_TO_SURFACE
$# cid title
$# ssid msid sttyp msttyp sboxid mboxid spr mpr
    1000000 1000001 3     3     0     0     0     0
$# fs fd dc vc vdc penchk bt dt
    0.0   0.0   0.0   0.0   0.0   0.0   0.0   0.0
$# sfs sfnm sst mst sfst sfnt fsf vsf
    1.0   1.0   0.0   1.0   1.0   1.0   1.0   1.0
                                         1           Ball to Plate
$# ssid msid sttyp msttyp sboxid mboxid spr mpr
    1000000 1000000 3     3     0     0     0     0
$# fs fd dc vc vdc penchk bt dt
    0.3   0.1   0.0   0.0   0.0   0.0   0.0   0.0
$# sfs sfnm sst mst sfst sfnt fsf vsf
    1.0   1.0   0.0   0.0   1.0   1.0   1.0   1.0
$ materials and thickness settings of tube, and connecting them by the keyword
*PART
$#
$# pid secid mid eosid hgid grav adpopt tmid
    1000000 1000000 1000000 0     0     0     0     0
*SECTION_SHELL_TITLE
boat
$# secid elform shrif nip propt q/r/rid icomp setyp
    1000000 2     1.0   5     1.0   0     0     0     1
$# tl t2 t3 t4 nloc marea idof edgset
    0.711 0.711 0.711 0.711 0.0   0.0   0.0   0.0
*MAT_PLASTIC_KINEMATIC_TITLE
subm
$# mid ro e pr sigy etan beta
    10000002.77900E-6 69.6 0.3   0.292 0.0   0.11
$# src spf fs vp
    0.0   0.0   0.7   0.0
$ Setting material parameters and thickness of plug , connect them by
the keyword
*PART
$#
$# pid secid mid eosid hgid grav adpopt tmid
    1000001 1000001 1000001 0     0     0     0     0
*SECTION_SOLID
$# secid elform aet
    1000001 1     0
*MAT_PLASTIC_KINEMATIC_TITLE
Tube
$# mid ro e pr sigy etan beta
    10000017.75000E-6 205.0 0.28 0.552 0.0   0.11
$# src spf fs vp
    0.0   0.0   0.35 0.0
*END
$ contact of tube self
*CONTACT_AUTOMATIC_SURFACE_TO_SURFACE_ID
$# cid title

```

## C2. Keywords for models with water and air

### C.2 Keywords for models with water and air

```

*KEYWORD MEMORY=200000000
*TITLE
*CONTROL_MPP_DECOMPOSITION_DISTRIBUTE_ALE_ELEMENTS
$ settings of termination time
*CONTROL_TERMINATION
$# endtim endcyc dmin endeng endmas nosol
  2.0   0   0.0  0.0100000E8  0
$ setting output data
*DATABASE_TRIHIST
$# dt binary lcur ioopt
1.00000E-4  0   0   1
*DATABASE_BINARY_D3PLOT
$# dt fcdt beam npltc psetid
  0.05  0   0   0   0
$# ioopt
  0
$ When a Lagrangian mesh overlaps with an Eulerian or ALE mesh, the
fluid structure (or ALE-Lagrangian) interaction is often modeled using
the *CONSTRAINED_LAGRANGE_IN_SOLID card, here the tube
mesh overlaps with the water mesh
*CONSTRAINED_LAGRANGE_IN_SOLID
$# slave master sstyp mstyp nquad ctype direc mcoup
  11 100  0   1   2   4   3   0
$# start end pfac fric frmin norm normtyp damp
  0.0100000E10 0.1  0.0  0.5  0   0   0.0
$# cq hmin hmax ileak pleak lcipor nvent blockage
  0.0  0.0  0.0  1   0.5  0   0   0
$# iboxid ipenck inforc ialeso lagmul pfacmm thkf
  0   0   0   0   0.0  0   0   0.0
*ALE_MULTI-MATERIAL_GROUP
$# sid idtype gpname
  1   1air
  2   1water
$ contact settings of the tube and plugs
*CONTACT_AUTOMATIC_SINGLE_SURFACE_ID
$# cid title
  1
$# ssid msid sstyp mstyp sboxid mboxid spr mpr
  11  0   2   0   0   0   0   0
$# fs fd dc vc vdc penchk bt dt
  0.6  0.0  0.0  0.0  0.0  0   0.0100000E20
$# sfs sfm sst mst sfst sfnt fsf vsf
  1.0 1.0  0.0  0.0  1.0  1.0  1.0  1.0
**SET_PART_LIST_TITLE
Tube
$# sid da1 da2 da3 da4 solver
  11 0.0  0.0  0.0  0.0MECH
$# pid1 pid2 pid3 pid4 pid5 pid6 pid7 pid8
  11 12 13  0   0   0   0   0
$ ALE solver settings, set global control parameters for the ALE and
Eulerian calculations.
*CONTROL_ALE
$# det nadv meth afac bfac cfac dfac efac
  -1  1   1   -1.0 0.0  0.0  0.0  0.0
$# start end aafac vfact prit ebc pref nsidbc
  0.0100000E20 1.0100000E-6 0   0   0.00466  0
$# ncpl nbkt imasc1 checkr beamin mmgpref pdifmx dtmfac
  1   50  0   0.0  0.0  0   0.0  0.0
$ parameter settings of air

```

```

Plug1
$# pid secid mid eosid hgid grav adopt tmid
 12 12 12 0 0 0 0 0 0
*SECTION_SHELL_TITLE
plug
$# secid elform shrf nip propt qr/irid icomp setyp
 12 2 1.0 5 1.0 0 0 0 1
$# t1 t2 t3 t4 nloc marea idof edgset
 0.711 0.711 0.711 0.711 0.0 0.0 0.0 0.0 0
*PART
$#
          title
Plug2
$# pid secid mid eosid hgid grav adopt tmid
 13 12 12 0 0 0 0 0 0
*MAT_RIGID_TITLE
plug
$# mid ro e pr n couple m alias
 12 7.664E-5 70.0 0.33 0.0 0.0 0.0
$# cmo con1 con2
 1.0 4 0
$#lco or a1 a2 a3 v1 v2 v3
 0.0 0.0 0.0 0.0 0.0 0.0
$Define damping
*DAMPING_FREQUENCY_RANGE
$# cdamp flow fhigh psid blank pidrel
 0.05 5.0 1000.0 0 0 0
*DAMPING_PART_MASS
$# pid lcid sf flag
 1 1 1.0 0
*DAMPING_PART_MASS
$# pid lcid sf flag
 2 1 1.0 0
*DEFINE_CURVE
$# lcid sidr sfa sfo offa offo dattyp lcint
 1 0 1.0 1.0 0.0 0.0 0 0
$#
  a1 o1
  0.0 200.0
  0.02 100.0
  0.04 50.0
  0.06 20.0
  0.08 10.0
  0.1 5.0
  0.12 2.0
  0.14 1.0
  0.16 1.0
  2.05 1.0
$ define the area of water (outside the tube and plugs) and air (inside the tube)
*INITIAL_VOLUME_FRACTION_GEOMETRY
$# fmsid fmtdtyp bammg ntrace
 100 1 2 8
$# conttyp filopt fammg vx vy vz radvel unused
 1 0 1 0.0 0.0 0.0 0
$# sid stype normdir xoffset unused unused unused unused
 14 1 0 0.0
$ define Non-reflecting boundary condition
*BOUNDARY_NON_REFLECTING
$# ssid ad as
 1 0.0 0.0
*SET_SEGMENT_GENERAL_TITLE
Non-reflective boundary
$# sid da1 da2 da3 da4 solver
 1 0.0 0.0 0.0 0.0MECH
$# option msrid xmin xmax ymin ymax zmin zmax
SALEFAC 1 1 1 0 0 0 0 0
SALEFAC 1 251 251 0 0 0 0 0
SALEFAC 1 0 0 1 1 0 0 0
SALEFAC 1 0 0 301 301 0 0 0
SALEFAC 1 0 0 0 0 1 1 1
SALEFAC 1 0 0 0 0 251 251
*END

```

## References

- [1] Wikipedia. ARA San Juan (S-42), the free Encyclopedia. 2019a. Online; accessed 2-August-2019; [https://en.wikipedia.org/wiki/ARA\\_San\\_Juan\\_\(S-42\)](https://en.wikipedia.org/wiki/ARA_San_Juan_(S-42)).
- [2] Wikipedia. The Manhattan project, the free Encyclopedia. 2019b. Online; accessed 1-August-2019; [https://en.wikipedia.org/wiki/Manhattan\\_Project](https://en.wikipedia.org/wiki/Manhattan_Project).
- [3] Wikipedia. Building implosion, the free Encyclopedia. 2019c. Online; accessed 11-July-2019; [https://en.wikipedia.org/wiki/Building\\_implosion](https://en.wikipedia.org/wiki/Building_implosion).
- [4] Orr M, Schoenberg M. Acoustic signatures from deep water implosions of spherical cavities. J Acoust Soc Am 1976;59:1155–9.
- [5] Wikipedia. Super-Kamiokande, the free Encyclopedia. 2019d. Online; accessed 20-August-2019; <https://en.wikipedia.org/wiki/Super-Kamiokande>.
- [6] Fairbairn W. On the resistance of tubes to collapse. Philos Trans R Soc London 1858;148:389–413.
- [7] Isaacs JD, Maxwell AE. The ball-breaker, a deep water signalling device. J Mar Res 1952;11:63–8.
- [8] Urick RJ. Implosions as sources of underwater sound. J Acoust Soc Am 1963;35:2026–7.
- [9] Hunter KS, Geers TL. Pressure and velocity fields produced by an underwater explosion. J Acoust Soc Am 2004;115:1483–96.
- [10] Keller JB, Kolodner II. Damping of underwater explosion bubble oscillations. J Appl Phys 1956;27:1152–61.
- [11] Hilgenfeldt S, Brenner MP, Grossmann S, Lohse D. Analysis of Rayleigh-Plesset dynamics for sonoluminescing bubbles. J Fluid Mech 1998;365:171–204.
- [12] Gish LA. Analytic and numerical study of underwater implosion. Massachusetts Institute of Technology; 2013. Ph.D. thesis.
- [13] Ikeda CM. Fluid structure interactions: implosions of shell structures and wave impact on a flat plate. University of Maryland, College Park; 2012.

- [14] Korkolis YP, Kyriakides S. Inflation and burst of aluminum tubes. Part II: an advanced yield function including deformation-induced anisotropy. *Int J of Plast* 2008;24:1625–37.
- [15] Ikeda CM, Wilkerling J, Duncan JH. The implosion of cylindrical shell structures in a high-pressure water environment. *Proc Roy Soc A-Math Phys* 2013;469:20130443.
- [16] Turner SE, Ambrico JM. Underwater implosion of cylindrical metal tubes. *J Appl Mech* 2013;80:011013.
- [17] Kamran K. A compressible Lagrangian framework for the simulation of underwater implosion problems. Universitat Politècnica de Catalunya; 2013.
- [18] Farhat C, Wang KG, Main A, Kyriakides S, Lee LH, Chandar KR, et al. Dynamic implosion of underwater cylindrical shells: experiments and computations. *Int J Solids Struct* 2013;50:2943–61.
- [19] YouTube, by Kostack studio, submarine ARA San Juan Simulation (Implosion + Sinking). 2018. Online; uploaded 15-December-2018; [https://www.youtube.com/watch?v=QLF\\_yD-lpFO](https://www.youtube.com/watch?v=QLF_yD-lpFO).
- [20] Wikipedia. Blender (software), the free Encyclopedia. 2019e. Online; accessed 31-August-2019; [https://en.wikipedia.org/wiki/Blender\\_\(software\)](https://en.wikipedia.org/wiki/Blender_(software)).
- [21] Chen G, Wang YC, Perronet A, Gu C, Yao PF, Bin-Mohsin B, et al. The advanced role of computational mechanics and visualization in science and technology: analysis of the germanwings flight 9525 crash. *Phys Scripta* 2017;92:033002.
- [22] Wang K, Rallu A, Gerbeau JF, Farhat C. Algorithms for interface treatment and load computation in embedded boundary methods for fluid and fluid–structure interaction problems. *Int J Numer Meth Fl* 2011;67:1175–206.
- [23] Wang K, Grétarsson J, Main A, Farhat C. Computational algorithms for tracking dynamic fluid–structure interfaces in embedded boundary methods. *Int J Numer Meth Fl* 2012;70:515–35.
- [24] Day J. Guidelines for ALE modeling in LS-DYNA. Report. Livermore software technology corporation, Livermore, California, USA; 2009.
- [25] Chen H. LS-DYNA structured ALE(S-ALE) solver. In: 14th International LS-DYNA users conference, Livermore software technology corporation, Livermore, California, USA, 2016; 2016.
- [26] Lysmer J, Kuhlemeyer RL. Finite dynamic model for infinite media. *J Eng Mech Div* 1969;95:859–78.
- [27] Cohen M, Jennings P. Computational methods for transient analysis. Computational methods for transient analysis, North-Holland, New York. Belytschko T, Hughes TJR, editors; 1983.
- [28] LS-DYNA. LS-DYNA Theory manual, r:9320. Livermore, California, USA: Livermore software technology corporation; 2017.
- [29] LSTC. LS-DYNA R10.0 keyword manual vol. I. 2017. Online; accessed 16-October-2017; [http://ftp.lstc.com/anonymous/outgoing/jday/manuals/LS-DYNA\\_Manual\\_Volum\\_R10.0.pdf](http://ftp.lstc.com/anonymous/outgoing/jday/manuals/LS-DYNA_Manual_Volum_R10.0.pdf).
- [30] Sturm RG. A study of the collapsing pressure of thin-walled cylinders. Tech. Rep.. University of Illinois at Urbana Champaign, College of Engineering; 1941.
- [31] Singer J, Arbocz J, Weller T. Buckling experiments: experimental methods in buckling of thin-walled structures: shells, buildup structures, composites and additional topics, vol. 2. John Wiley & Sons, Inc.; 2002.
- [32] Farhat C, Rallu A, Shankaran S. A higher-order generalized ghost fluid method for the poor for the three-dimensional two-phase flow computation of underwater implosions. *J Comput Phys* 2008;227:7674–700.
- [33] Muttaqie T, Sohn JM, Cho SR, Park SH, Choi G, Han S, et al. Implosion tests of aluminium alloy tubes under external hydrostatic pressure. In: ASME 2018 37th International conference on ocean, offshore and arctic engineering. American society of mechanical engineers; 2018. p. 10.
- [34] Gupta S, LeBlanc JM, Shukla A. Mechanics of the implosion of cylindrical shells in a confining tube. *Int J Solids Struct* 2014;51:3996–4014.
- [35] Gupta S, Parameswaran V, Sutton MA, Shukla A. Study of dynamic underwater implosion mechanics using digital image correlation. *Proc Roy Soc A-Math Phys* 2014;470:20140576.
- [36] Gupta S, Matos H, Shukla A, LeBlanc JM. Pressure signature and evaluation of hammer pulses during underwater implosion in confining environments. *J Acoust Soc Am* 2016;140:1012–22.
- [37] Jaramillo H.S.. ARA San Juan S-42 – CAD forum. 2018. Online; accessed 14-November-2018; <https://grabcad.com/library/submarine-ssk-tr-1700-s42-ara-san-juan-1>.
- [38] HY-100 steel. 2017. Online; <https://www.diversifiedmetals.com/product/hy-100-steel/>.
- [39] Lin ZL, Liao SJ. Calculation of added mass coefficients of 3D complicated underwater bodies by FMBEM. *Commun Nonlinear Sci Numer Simul* 2011;16:187–94.
- [40] YouTube, by Kostack Studio, ARA San Juan simulation Dev Reel (Sim Failures & Glitches). 2019. Online; uploaded 21-December-2018; <https://www.youtube.com/watch?v=R-tlV3feDuQ&t=214s>.
- [41] Chen G, Gu C, Morris PJ, Paterson EG, Sergeev A, Wang YC, et al. Malaysia airlines flight MH370: water entry of an airliner. *Notices Amer Math Soc* 2015;62:330–4.
- [42] Tam CK. Computational aeroacoustics-issues and methods. *AIAA J* 1995;33(10):1788–96.
- [43] Sturt R.. Numerical damping algorithms in LS-DYNA. 2018. Online; accessed 17-January-2018; <https://www.dynasupport.com/howtos/general/damping/>.
- [44] Du N.. The speed of sound in water. 2000. Online; <https://hypertextbook.com/facts/2000/NickyDu.shtml>.
- [45] Tam CK. Computational aeroacoustics: a wave number approach, vol.-33. Cambridge University Press, U.K.; 2012.